

To Appear the in *The Astrophysical Journal*

Proton-Capture Nucleosynthesis in Globular Cluster Red Giant Stars

Robert M. Cavallo

Department of Astronomy, University of Maryland, College Park, MD 20742;
rob@astro.umd.edu

Allen V. Sweigart

Laboratory for Astronomy and Solar Physics, Code 681, NASA/Goddard Space Flight
Center, Greenbelt, MD 20771; sweigart@bach.gsfc.nasa.gov

and

Roger A. Bell

Department of Astronomy, University of Maryland, College Park, MD 20742;
roger@astro.umd.edu

ABSTRACT

Observational evidence suggests that many of the variations of the surface abundances of light to intermediate mass elements ($A < 28$) in globular cluster red-giant-branch (RGB) stars can be attributed to non-canonical mixing between the surface and the deep stellar interior during the RGB phase. As a first step to studying this mixing in more detail, we have combined a large nuclear reaction network with four detailed stellar evolutionary sequences of different metallicities in order to follow the production and destruction of the C, N, O, Ne, Na, Mg, and Al isotopes around the hydrogen-burning shell (H shell) of globular cluster RGB stars. The abundance distributions determined by this method allow for the variation in the temperature and density around the H shell as well as for the dependence on both the stellar luminosity and cluster metallicity. Because our nuclear reaction network operates separately from the stellar evolution code, we are able to more readily to explore the effects of the uncertainties in the reaction rates on the calculated abundances.

We discuss implications of our results for mixing in the context of the observational data. Our results are qualitatively consistent with the observed C vs. N, O vs. N, Na vs. O, and Al vs. O anticorrelations and their variations

with both luminosity and metallicity. We see evidence for variations in Na without requiring changes in O, independent of metallicity, as observed by Norris & Da Costa (1995a) and Briley et al. (1997). Also, we derive $^{12}\text{C}/^{13}\text{C}$ ratios near the observed equilibrium value of 4 for all sequences, and predict the temperature-dependent $^{16}\text{O}/^{17}\text{O}$ equilibrium ratio based on new data for the $^{17}\text{O}(p, \alpha)^{14}\text{N}$ reaction rate. Additionally, we discuss the Mg isotopic abundances in light of the recent observations of M13 (Shetrone 1996b) and NGC 6752 (Shetrone 1997).

Subject headings: globular clusters: general – nuclear reactions, nucleosynthesis, abundances – stars: abundances – stars: late-type – stars: interiors – stars: Population II

1. Introduction

Stars which lie near each other on the color-magnitude diagrams of globular clusters were initially thought to have similar chemical compositions. However, observations over the past two decades have shown a large scatter of the abundances of C, N, O, Na, Mg, and Al among cluster red-giant stars [for reviews, see Kraft (1994) and Briley et al. (1994)]. Explanations for these abundance variations have generally focused on two possibilities: 1) the mixing of nucleosynthesized material from the deep stellar interior during the red-giant-branch (RGB) evolution, and 2) primordial abundance variations within the globular cluster material. In this work we model those abundance variations which can be attributed to mixing during the red-giant-branch (RGB) evolution by using a detailed nuclear reaction network together with four RGB stellar evolutionary sequences of different metallicities. We make no attempt to model those variations which are likely the result of primordial contamination from prior stellar evolution, such as the observed Fe-peak metallicity spread in ω Cen (Dickens & Bell 1976), the Ca abundance variations in M22 (Anthony-Twarog, Twarog, & Craig 1995), and the Na variations on the upper main sequence of 47 Tuc (Briley et al. 1996).

The decrease in C with increasing luminosity seen in the very metal-poor ($[\text{Fe}/\text{H}]^1 \lesssim -2.0$) and intermediate metallicity ($-2.0 \lesssim [\text{Fe}/\text{H}] \lesssim -1.1$) clusters supports the mixing hypothesis. In the intermediate-metallicity and metal-rich ($[\text{Fe}/\text{H}] \gtrsim -1.1$) clusters where

¹This follows the notation: $[\text{X}] = \log(\text{X})_{\star} - \log(\text{X})_{\odot}$

^{13}C is also observable, the $^{12}\text{C}/^{13}\text{C}$ ratio is seen to decrease to near its equilibrium value as the luminosity increases, providing further evidence of mixing on the RGB. (Bell, Dickens, & Gustafsson 1979; Bell & Dickens 1980; Da Costa & Cottrell 1980; Carbon et al. 1982; Trefzger et al. 1983; Langer et al. 1986; Smith & Suntzeff 1989; Briley et al. 1990; Suntzeff & Smith 1991; Brown, Wallerstein, & Oke 1991). Along with these changes, observations of the CN and NH bands have shown that C is anticorrelated with N at all metallicities (Hesser, Hartwick, & McClure 1977; Norris & Freeman 1979; Norris et al. 1981; Suntzeff 1981; Langer, Kraft, & Friel 1985; Smith & Bell 1986). Furthermore, N and Na are both anticorrelated with O and their abundances are seen to increase with increasing luminosity (Cottrell & Da Costa 1981; Pilachowski 1988; Paltoglou & Norris 1989; Dickens et al. 1991; Sneden et al. 1991; Drake, Smith, & Suntzeff 1992; Sneden et al. 1992; Norris & Da Costa 1995a; Smith et al. 1996; Pilachowski et al. 1996; hereafter, PSKL96). The variations in Na, first found by Cohen (1978) and Peterson (1980), were not initially thought to be the result of internal stellar evolution; however, Denisenkov & Denisenkova (1990) and Langer, Hoffman, & Sneden (1993) showed that Na could be produced from proton captures on Ne at the same temperatures that O is destroyed.

The Al abundance also shows an anticorrelation with O, but with a stronger dependence on metallicity than Na (Norris & Da Costa 1995a; 1995b); some metal-poor clusters exhibit large Al enhancements by as much as 1.2 dex, while the more metal-rich clusters have no Al variations (Cottrell & Da Costa 1981). Langer, Hoffman, and Sneden (1993) showed that Al can be produced from proton captures on $^{25,26}\text{Mg}$, and subsequently, Langer & Hoffman (1995) attempted to explain the large Al overabundances in M13 (Kraft et al. 1997) by suggesting that the $^{25,26}\text{Mg}$ isotopes were initially overabundant by a factor of 2. However, the observations of Mg in M13 by PSKL96 and Shetrone (1995) do not support this conclusion.

The observations of the Mg abundances show the most erratic trends. PSKL96 showed that fainter red giants with small (< 0.10 dex) Na enhancements had large Mg abundances. However, while roughly half of the giants with large Na enhancements had low Mg, the rest were widely distributed in Mg abundance, by ~ 0.6 dex. For the high luminosity giants, most were Na-enriched while, on the other hand, more than half showed no evidence of Mg depletion. The difficulty in describing the Mg abundance observations stems from the fact there are three stable Mg isotopes which are relatively plentiful; e.g., $\log(\text{N}(\text{Mg})/\text{N}(\text{H}))_{\odot} = -4.42$ with the $^{24}\text{Mg}:^{25}\text{Mg}:^{26}\text{Mg}$ ratio equal to 79:10:11 on earth and presumably in the solar photosphere (Anders & Grevesse 1989). Shetrone (1996a, 1996b) argued that the change in the total Mg abundance for M13 giants near the RGB tip is controlled by ^{24}Mg by demonstrating that ^{24}Mg is anticorrelated with Al. Other studies have shown total Mg vs. CN anticorrelations in ω Cen (Norris & Da Costa 1995a) and NGC 6752 (Shetrone

1997), while still other studies found no star-to-star variations in Mg in NGC 6752, 47 Tuc, or M22 (Hesser 1978; Norris et al. 1981; Smith & Wirth 1991; Briley, Hesser, & Bell 1991). In this work, we look at how the changes in these elemental abundances could be brought about during a star’s ascent up the RGB.

There have been some theoretical attempts to explain these abundance variations. For example, Sweigart & Mengel (1979; hereafter, SM79) showed that there were regions above the hydrogen-burning shell (H shell) where C and O were depleted. They suggested that rotationally driven meridional circulation on the RGB could transport material from these depleted regions to the outer convective envelope. Their work qualitatively accounted for the C and O vs. N anticorrelations as well as the decline in C and the $^{12}\text{C}/^{13}\text{C}$ ratio with increasing luminosity. Although they used detailed stellar models of different metallicities, they lacked a full reaction network to study the variations in the elements beyond O and did not examine the uncertainties in the nuclear reaction rates.

Denissenkov & Weiss (1996) recently examined deep diffusive mixing in globular cluster and halo giants by constructing a very metal-poor ($Z = 0.0004$) stellar sequence containing four models and combining it with the widely used rates of Caughlin & Fowler (1988; hereafter, CF88). They used a two-parameter mixing scenario; one which controlled the mixing depth and the other which controlled the mixing rate. They were able to model the observed changes in the $^{12}\text{C}/^{13}\text{C}$ ratio and $[\text{C}/\text{Fe}]$ with M_V in M92 as well as the global O vs. Na anticorrelation observed in other clusters such as M3 and M13 (Kraft et al. 1992, 1993; hereafter, KSLP92 and KSLS93, respectively). However, each correlation required a different set of parameters, and they were still unable to reproduce the large enhancement of ^{27}Al seen in some clusters without increasing the initial $^{25,26}\text{Mg}$ abundances beyond the scaled solar value. These difficulties may be due to the fact that they only considered a single sequence and were therefore unable to discuss metallicity-dependent variations. Furthermore, their use of the CF88 reaction rates did not allow them to take advantage of the updated data for the NeNa and MgAl cycles, which have changed substantially since the work of CF88.

In our previous study (Cavallo, Sweigart, & Bell 1996; hereafter, Paper I), we used an extensive nuclear reaction network to compute the isotopic abundances around the H shell during the RGB evolution of two stellar model sequences of different metallicities. The conclusions from Paper I were that ^{23}Na is produced first by proton captures on ^{22}Ne in the region where O begins to deplete, then from ^{20}Ne via the NeNa cycle deeper in the region of O depletion. Further, ^{27}Al is produced in the O-depleted region by proton captures, first on $^{25,26}\text{Mg}$, then on ^{24}Mg in the MgAl cycle (see Fig. 1 of Paper I for a graphical description of the NeNa and MgAl cycles). However, the replenishment of ^{24}Mg by proton captures on

^{23}Na occurred at a faster rate than its depletion to form ^{27}Al . Thus, while the results were in qualitative agreement with the observations for Na and Al, they could not predict the observed Mg variations.

In this paper, we extend the work of Paper I by examining more fully the effects of the nuclear reaction rates and stellar structure on the abundance profiles of C, N, O, Na, Mg, and Al around the H shell along four RGB stellar evolutionary sequences. Our approach will include the effects of the variation in the temperature and density around the H shell on the isotopic abundance yields. In addition, we will follow the changes in the abundances as the H shell evolves. Finally, by using a detailed nuclear reaction network that is separate from the stellar evolutionary code, we can explore the uncertainties in the reaction rates easily and efficiently. We make no attempt to incorporate mixing at this stage and concentrate, instead, on the development of the abundance profiles in the sequences.

In section 2 we describe the computational procedure used both here and in Paper I. We discuss the role of temperature and density in controlling the shape and lifetime of the abundance profiles around the H shell in section 3. Our results for the abundance profiles are presented in section 4, while in section 5 we examine these results in the context of mixing. In section 6 we explore the impact of the uncertainties in the nuclear reaction rates on our results, and in section 7 we summarize the observational implications of our results.

2. Computational Procedure

2.1. Stellar Evolutionary Sequences

We have computed four stellar evolutionary sequences, three which cover the range of metallicities seen in the globular clusters and one which corresponds to an old disk star with solar metallicity. The masses of the globular cluster sequences are chosen to give an age of ~ 15 Gyr at the tip of the RGB. Since the evolution up the RGB does not depend strongly on the mass of the star, the choice of age does not significantly affect our results. The sequences are begun at the zero-age main sequence and evolved up the RGB to the He flash at the tip of the RGB. The input physics for these model computations is outlined in Sweigart (1997a). The properties of the sequences are given in Table 1. They contain from 1600 to 4000 models between the onset of mixing, as discussed below, and the He flash. From these we have selected models at increments of $0.005 M_{\odot}$ in M_{sh} , where M_{sh} is the mass interior to the H shell, or, equivalently, the mass of the helium core. Each model provides us with the run of temperature and density around the H shell as well as the hydrogen-shell luminosity, effective temperature, and age.

A fundamental question is to decide where along the RGB to begin the mixing process. As discussed by SM79, the hydrogen discontinuity left behind by the deep penetration of the convective envelope during the first dredge-up probably prevents the circulation currents from accessing the regions of C-N and O-N conversion. However, once the H shell has burned past this discontinuity, the currents are no longer inhibited by a mean molecular weight gradient, and hence, the region above the H shell can then be mixed. This point along the RGB corresponds to the well-known bump in the RGB luminosity function (Fusi Pecci et al. 1990). This hypothesis appears to be supported by the work of Richard et al. (1996) who showed that there is a critical μ -gradient in the sun which is sufficient to stop rotationally induced circulation of matter. The results of Bell, Dickens, & Gustafsson (1979) add observational evidence to this assumption. Gilroy & Brown (1991) have demonstrated that in the old open cluster M67 ($[\text{Fe}/\text{H}] \sim 0$) the $^{12}\text{C}/^{13}\text{C}$ ratio does not begin to decline past its canonical value until the predicted start of mixing. Likewise, Suntzeff (1981) notes that the abundances in M3 giants appear to follow the SM79 presumption, but those in M13 don't. Furthermore, Charbonnel (1994, 1995) has successfully modeled the observed variation of $^{12}\text{C}/^{13}\text{C}$, ^7Li , and $^{12}\text{C}/^{14}\text{N}$ in both globular and open clusters under this assumption.

There are, however, observations which show that abundance anomalies persist at luminosities below the point at where the H shell burns through the hydrogen discontinuity. In addition to the previously noted Na variations seen in 47 Tuc, some observers have seen star-to-star differences in the CN content of lower RGB and sub-giant-branch (SGB) stars in the clusters M3, M4, M5, M92, NGC 6752, and 47 Tuc (Bell, Hesser, & Cannon 1983; Norris & Smith 1984; Langer et al. 1986; Smith, Bell, & Hesser 1989; Suntzeff & Smith 1991; Briley et al. 1992). In these cases, the CH band strength appears to be weakly anticorrelated with the CN band strength. However, at these lower luminosities, the G band of CH is difficult to measure with the necessary accuracy to ascertain the CH abundance (Bell, Hesser, & Cannon 1984). As pointed out by Vandenberg & Smith (1988), the best hope of diagnosing the inherent nature of the CN anomalies (primordial or mixing) is to measure the $^{12}\text{C}/^{13}\text{C}$ ratio, which drops sharply at the onset of mixing. At present, there is a paucity of data concerning this ratio at such low luminosities.

In this work we will assume that mixing begins at the point along the RGB where the H shell burns through the hydrogen discontinuity and save an investigation into mixing on the lower RGB and SGB for another project.

2.2. Nuclear Reaction Network

Our nuclear reaction network was kindly supplied by Dr. David Arnett of the University of Arizona. The original version relied mostly on the rates of CF88; we have since modified the code to reflect more modern results for the rates in the CNO, NeNa, and MgAl cycles at the temperatures around the H shell of our models. We discuss the reaction rates in detail and examine the effects of their uncertainties on our results in section 6.

This network code requires three input ingredients: the run of temperature and density around the H shell, the initial envelope composition, and the timescale for the nuclear reactions. The last ingredient is obtained by the stationary shell approximation which is discussed in the following subsection. As indicated above, we obtain the run of temperature and density from the RGB models.

We supply an initial composition for all isotopes from F through Ca according to their scaled solar abundance (Anders & Grevesse 1989). The envelope values of the C, N, and O isotopes are given by the models and include the effects of the first dredge-up at the base of the RGB. The network follows the reactions of 113 nuclei from ^1H to ^{49}Ca and produces the abundance profiles in the region of the H shell for each model.

2.3. Stationary Shell Approximation

There are two ways to compute the distribution of the elements around the H shell. The most direct method is to incorporate the nuclear reaction network into the stellar evolution code. This becomes very expensive computationally, especially when trying to explore the uncertainties in the various reaction rates. A simpler method is to derive the models first and then to compute the composition distribution afterwards via the stationary shell approximation (SSA), which we outline here. In addition to being more computationally efficient, the SSA also allows us to vary the reaction rates, and (later) the mixing algorithm parameters, without having to recompute each evolutionary sequence.

In order to integrate the network code, one must know the timescale of the nuclear burning. This burning time can be straightforwardly determined through the use of the SSA, as we now demonstrate. Figure 1 shows the H-shell profile at two different times, t_1 and t_2 . At an arbitrary point in the shell the hydrogen abundance decreases from X_1 at time t_1 , to X_2 at time t_2 according to the relation:

$$\Delta X = X_1 - X_2 = \frac{dX}{dt} \Delta t, \quad (1)$$

where $\Delta t = t_2 - t_1$ is the burning time. *Provided that the shell profile does not change*

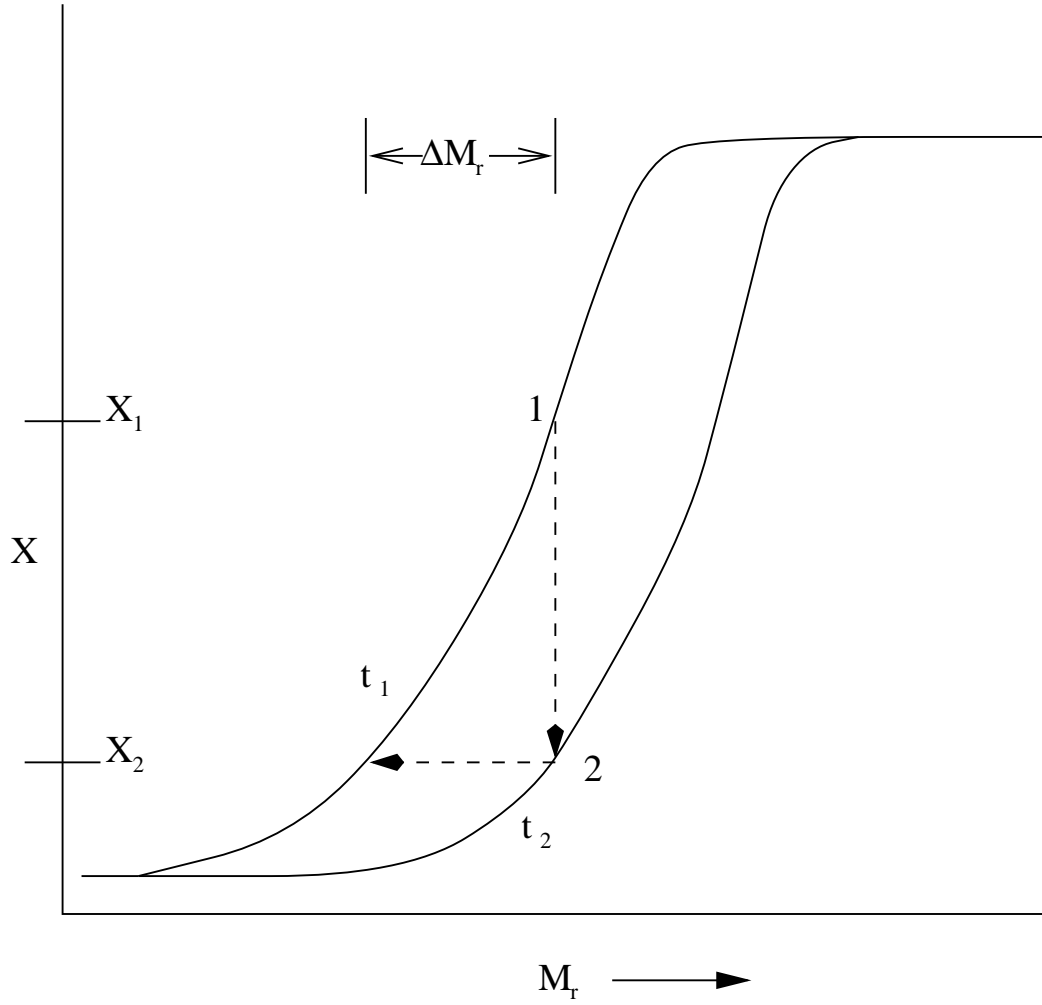


Fig. 1.— Schematic diagram of the H shell at two different times t_1 and t_2 .

significantly over the time interval Δt , we can also compute the change in X from the equation:

$$\Delta X = \frac{dX}{dM_r} \Delta M_r, \quad (2)$$

where ΔM_r is the amount of mass through which the H shell advances over the time interval Δt . Thus, changing from X_1 to X_2 can be accomplished either by remaining at a fixed value of the mass coordinate M_r and allowing the shell to advance outward over a time Δt , or by integrating along the profile over the mass interval ΔM_r .

The next step is to relate Δt to ΔM_r . Letting X_e denote the envelope hydrogen abundance, it follows that the mass of hydrogen, ΔM_X , burned over the time interval Δt can be written as

$$\Delta M_X = (\Delta M_r) X_e.$$

Since the energy liberated by burning this mass of hydrogen must be equal to the total energy output of the shell over the time interval Δt , we can write

$$(\Delta M_r) X_e E = L_H \Delta t, \quad (3)$$

where E is the energy released in burning one gram of hydrogen and L_H is the hydrogen shell luminosity. Combining equations (1) - (3) yields the desired relationship

$$\frac{dX}{dt} = \frac{L_H}{X_e E} \frac{dX}{dM_r}. \quad (4)$$

Using equation (4), we can convert the time derivative of the hydrogen abundance, or any other isotopic abundance, as given by the nuclear reaction rates, to the corresponding derivative with respect to M_r . From this we can then determine the abundance distribution of the all of the isotopes around the H shell.

How well does the SSA work? In Figure 2 we compare the H and CNO abundances found with the SSA for a representative RGB model with the abundances computed with the stellar evolutionary code (see, e.g., Clayton 1983). The agreement is excellent at all points and justifies the use of the SSA to set the nuclear burning time.

3. Properties of the H shell

The isotopic abundance profiles around the H shell depend on the run of temperature and density and on the timescale, τ_{shell} , with which the shell advances outward in mass. In this section we discuss each of these in turn.

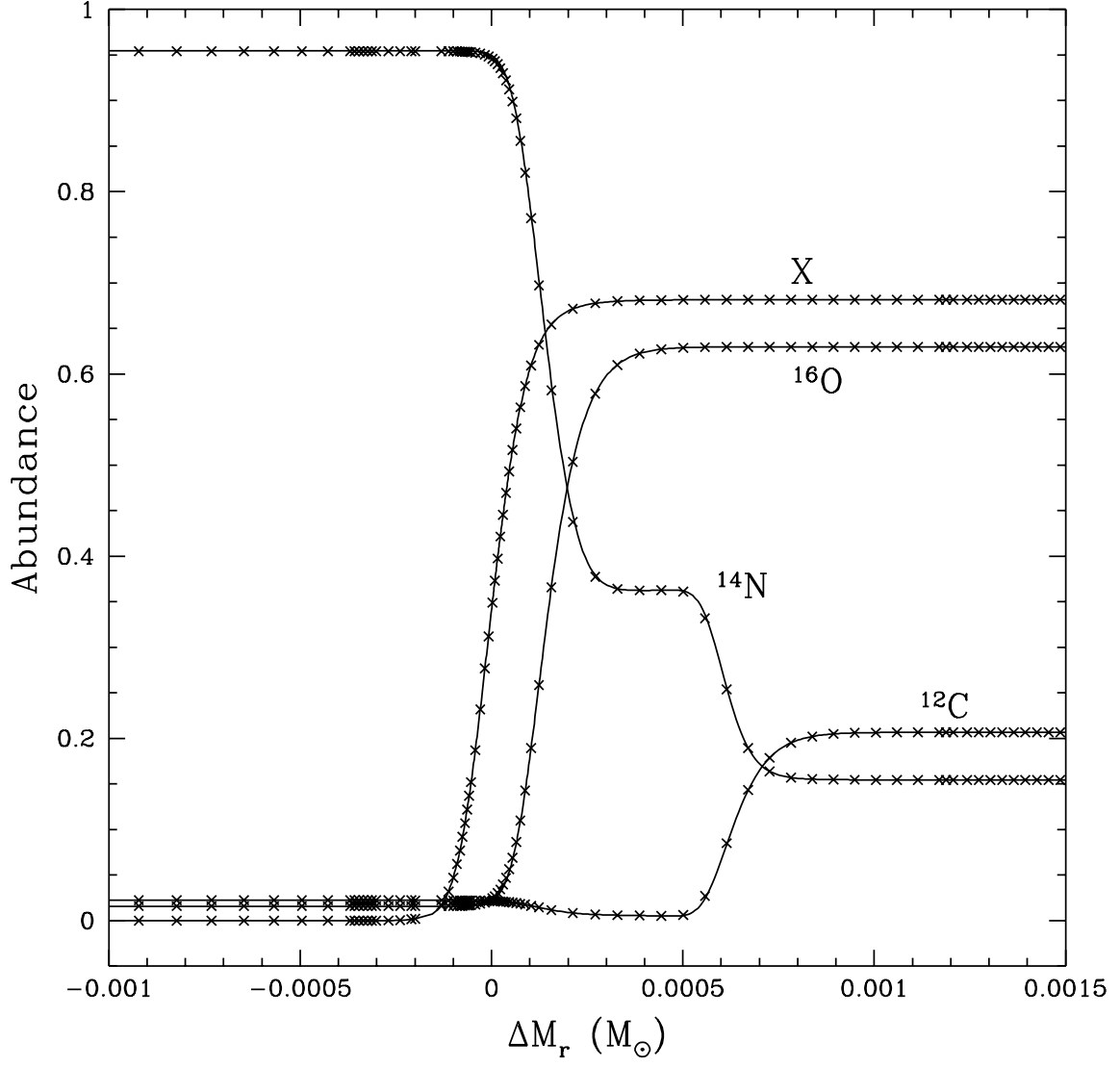


Fig. 2.— Comparison between the H and CNO abundances computed with the stationary shell approximation (x's) and the stellar code (solid line) for a representative RGB model. The ordinate is the number abundance relative to all metals. The curve labeled by X is the hydrogen-mass fraction on the same scale. The abscissa is the mass difference between any point and the center of the H shell.

3.1. Run of T and ρ around the H shell

In Figure 3a we plot the temperature profiles around the H shell for the $Z = 0.0004$ sequence at four values of M_{sh} . In order to explore various mixing algorithms, one would like to be able to interpolate accurately between these temperature profiles for an arbitrary point along the RGB. However, interpolating between these profiles is difficult due to their overlapping just above the H shell. In order to remedy this problem, we introduce the variable ΔS , defined by

$$\Delta S = \Delta M_r / \Delta M_H,$$

where $\Delta M_r = M_r - M_{\text{sh}}$ is the mass difference between any point and the center of the H shell, and ΔM_H is the thickness of the H shell, defined as the mass between the points where the H-mass fraction, X , is 10% ($\Delta S = -0.5$) and 90% ($\Delta S = +0.5$) of its envelope value. Panel (b) of Figure 3 demonstrates that using ΔS keeps the temperature curves separated near the H shell.

In Figure 4 we demonstrate the full range of temperatures around the H shell for all four sequences by plotting $T_9 (= T/10^9\text{K})$ as a function of ΔS at the start of mixing (top panel) and at the onset of the helium flash (bottom panel). The higher shell temperatures toward the tip of the RGB allow the occurrence of some nuclear reactions that were not possible lower down the RGB. In addition, the metal-poor sequences reach higher temperatures in the shell and allow some elements to undergo nuclear processing that would otherwise not be burned in the higher metallicity stars.

The density around the H shell for the same models plotted in Figure 3 is shown in Figures 5a and 5b. Again, by using ΔS we find that the density profiles near the H shell vary much more smoothly during the evolution. Although the density varies over many orders of magnitude near the H shell, its influence on the burning rates around the shell is only linear and, therefore, much less significant than the temperature dependence. The density typically ranges from ~ 0.01 to 1000 g cm^{-3} for all four sequences.

3.2. τ_{shell}

In addition to their dependence on temperature and density, the composition profiles also depend on the timescale with which the shell burns outward in mass. We call this quantity τ_{shell} and define it as the time required for the shell to move through one shell thickness, ΔM_H . The dependence of this timescale on luminosity is given in Figure 6a for the portion of each sequence where mixing is presumed to occur. The corresponding dependence of the hydrogen-burning luminosity, L_H , on the core mass, M_{sh} , is shown in

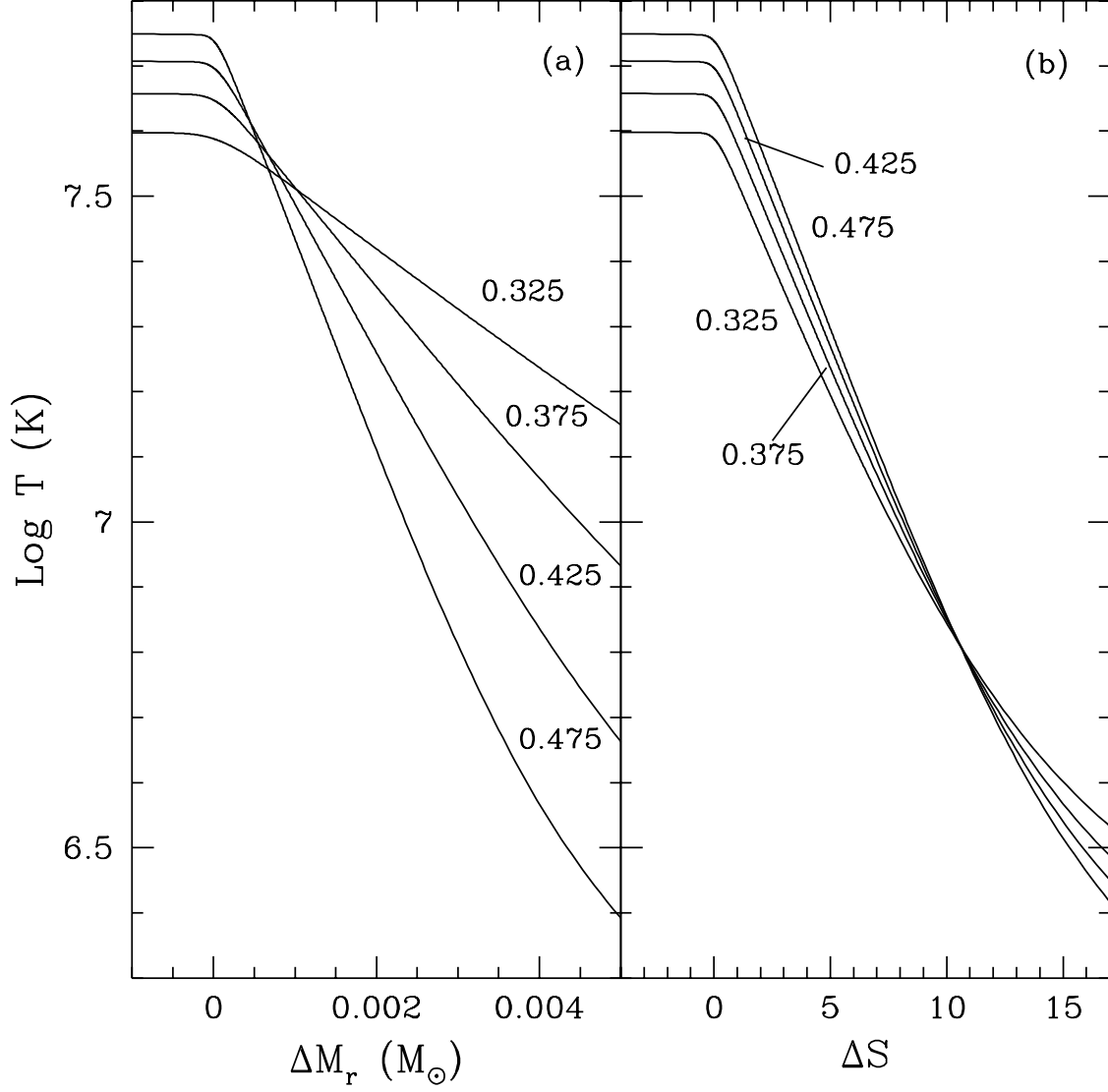


Fig. 3.— (a) Temperature profiles around the H shell as a function of the mass difference ΔM_r between any point and the center of the H shell for four models from the $Z = 0.0004$ sequence. Each curve is labeled by the mass, M_{sh} , interior to the H shell. (b) The same profiles, except as a function of ΔS .

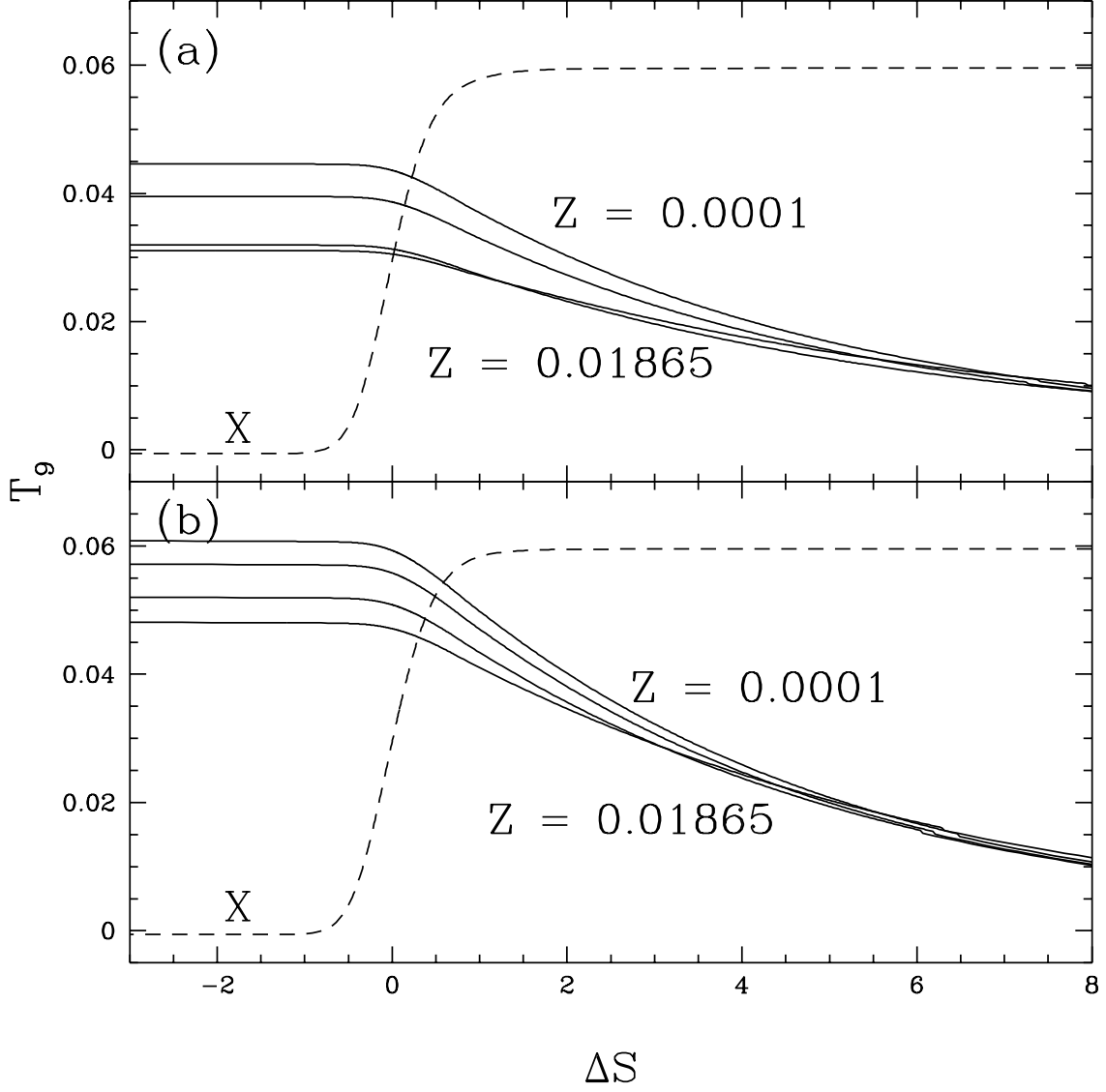


Fig. 4.— The range in temperature, T_9 , around the H shell for all four sequences at (a) the assumed onset of mixing and (b) the tip of the RGB. The dashed line is the hydrogen-mass fraction on an arbitrary scale.

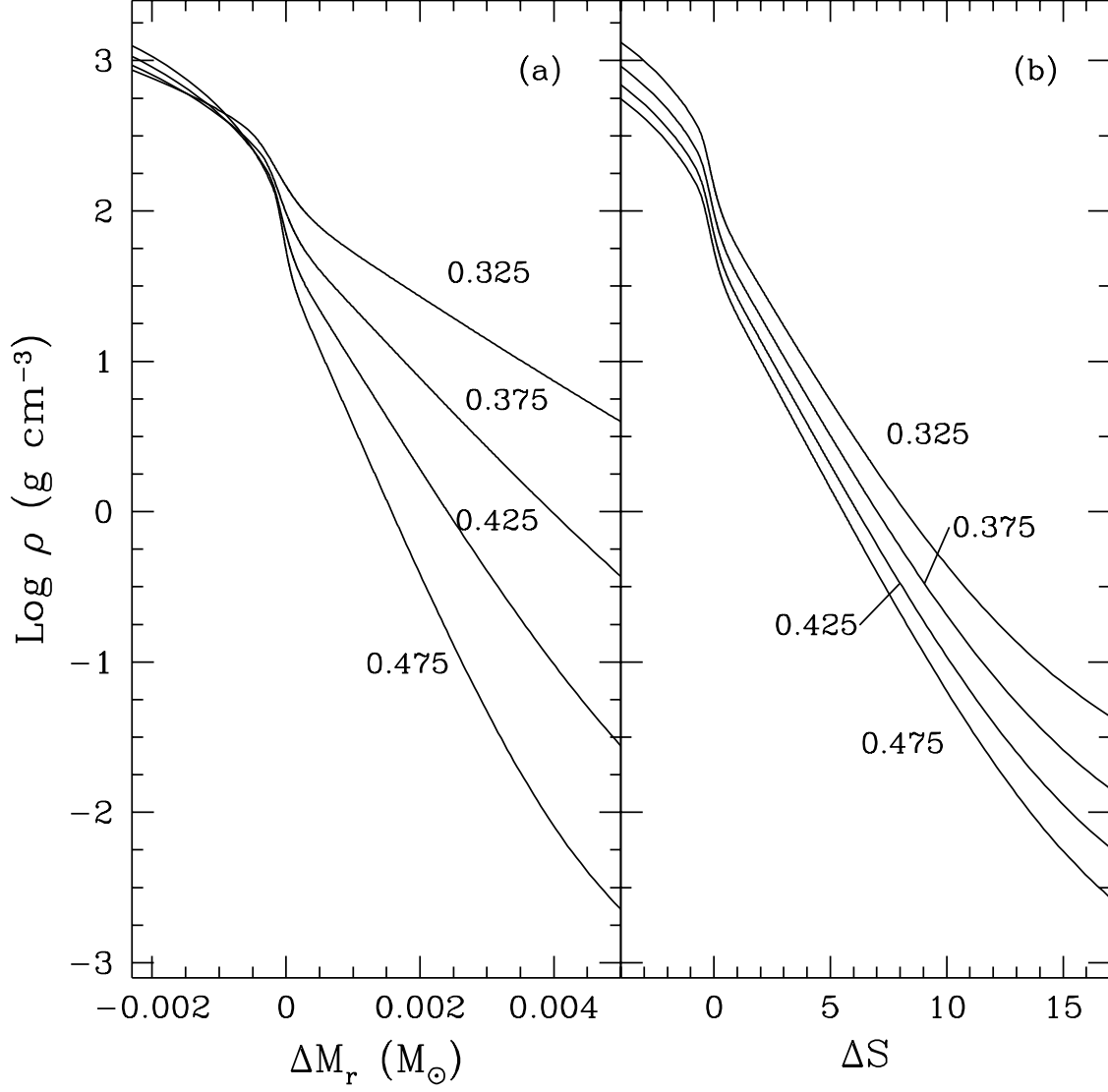


Fig. 5.— As Figure 3, but for the density.

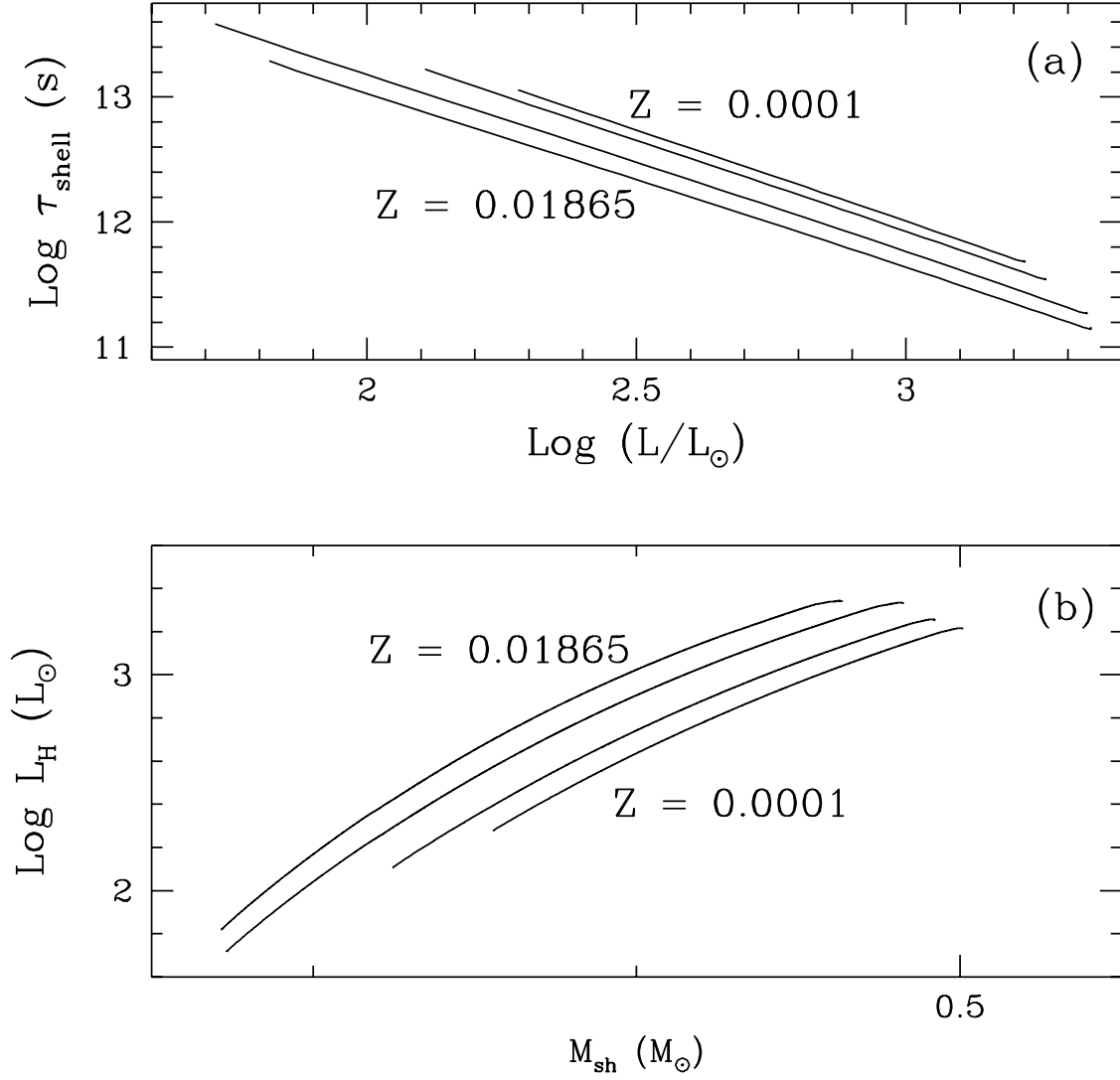


Fig. 6.— (a) The shell burning timescale, τ_{shell} , as a function of luminosity for the four stellar evolutionary sequences. (b) The hydrogen-burning luminosity as a function of the mass, M_{sh} , interior to the H shell for the same sequences.

Figure 6b. We see from this panel that at a given core mass, the higher metallicity sequences have a greater hydrogen burning luminosity due to a larger number of CNO nuclei. This increase in luminosity with metallicity, together with the increase in the luminosity with evolution up the RGB, translates into a shorter τ_{shell} , as shown explicitly in panel (a). Thus the higher metallicity and more evolved stars have less time to set up the composition profiles above the H shell.

The shell-burning timescale also depends on the shell thickness ΔM_{H} , which is plotted in Figure 7 as a function of M_{sh} for each metallicity. As a sequence evolves, the increase in the luminosity causes the temperature gradient across the H shell to steepen. As a consequence the shell burning region narrows with evolution. Moreover, the more metal-rich stars have steeper temperature gradients due to their larger opacities and greater flux, and thus, have narrower H shells at a given value of M_{sh} . Therefore, at brighter luminosities and higher metallicities, one expects the nuclear processing to occur in narrower burning regions, as implied by Figure 7.

4. Isotopic Abundance Profiles

The nuclear reaction network code produces the abundance profiles around the H shell for any isotope followed in the network. Here we discuss the profiles of the CNO-cycle elements first, then the NeNa- and MgAl-cycle elements.

4.1. C-N-O

Figures 8 - 11 give the C, N, and O profiles around the H shell of our sequences, at the start of mixing (top panels) and at the tip of the RGB (bottom panels). Above the H shell in each sequence is a region of C depletion in which the temperature is hot enough only to convert ^{12}C to ^{14}N in the CN cycle. Closer in toward the H shell there exists an O-depleted region where ^{16}O is converted into ^{14}N in the ON cycle. The narrowing of the C- and O-depleted regions with increasing luminosity is seen between the top and bottom panels in each of these figures. For example, at the onset of mixing in the $Z = 0.0004$ sequence (Figure 9a), C depletion occurs at $\Delta M_{\text{r}} = 0.0035 M_{\odot}$. As the sequence evolves to the tip of the RGB, ^{12}C begins to be depleted much closer to the H shell, near $\Delta M_{\text{r}} = 0.001 M_{\odot}$. A similar narrowing of the C- and O-depleted regions occurs when the metallicity increases. For example, the $Z = 0.0004$ sequence at the start of mixing (Figure 9a) experiences a depletion of ^{16}O around $\Delta M_{\text{r}} = 0.0015 M_{\odot}$ while the $Z = Z_{\odot}$ sequence (Figure 11a) depletes

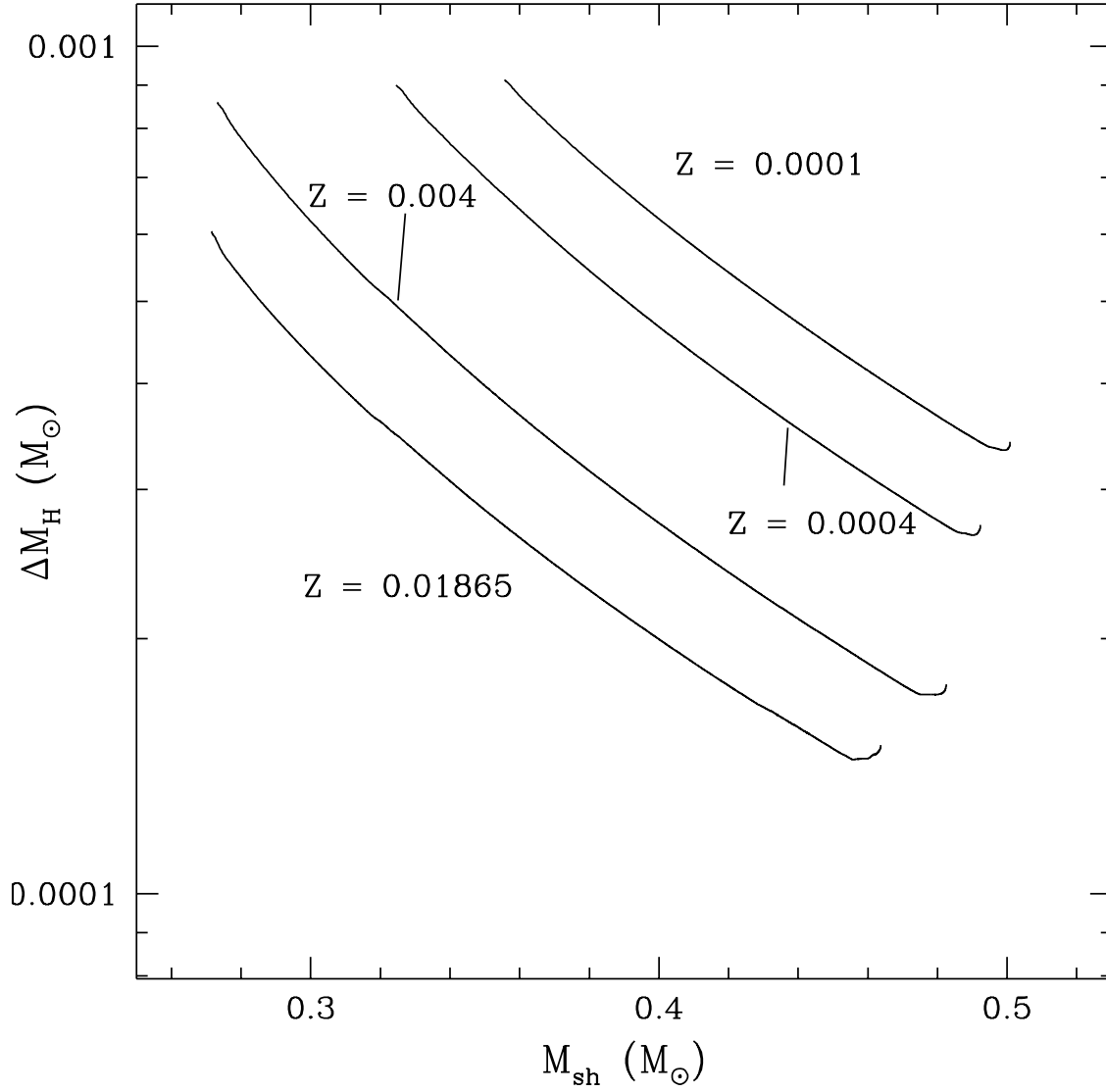


Fig. 7.— The shell thickness, ΔM_{H} , as a function of the mass, M_{sh} , interior to the H shell for the four evolutionary sequences. The small upturn near the tip of the RGB is due to the onset of the helium flash.

^{16}O much closer to the H shell at $\Delta M_r = 0.0005 M_\odot$.

The narrowing of the C- and O-depleted regions is compared in greater detail in Figure 12 for all the sequences at the points along the RGB where mixing is assumed to occur. As the sequences evolve, the C- and O-depleted regions occupy less mass above the H shell. This limits the amount of matter that can be processed and requires that the mixing penetrate closer to the H shell to reach the synthesized material. In addition, we see that higher metallicities reduce the breadth of the regions above the H shell from which synthesized matter can be mixed outward, as also found by SM79.

From the previous section we know that the narrowing of the C- and O-depleted regions during the evolution up the RGB is accompanied by a steepening of the H-shell profile. This suggests that the substantial narrowing of these regions during the RGB evolution might be less apparent if the CNO abundances are plotted in terms of the quantity ΔS [given in equation (5)], since ΔS measures mass difference in units of the H-shell thickness. We illustrate this point in Figure 13, where we show the CNO abundance profiles at both the start of mixing and the tip of the RGB for the $Z = 0.0004$ sequence. We see that these CNO abundance profiles are nearly invariant during the RGB evolution when plotted as a function of ΔS . This invariance is useful when comparing and interpolating abundances between models of a single sequence. In addition, ΔS naturally lends itself to discussions of mixing depth. For example, the “top,” “center,” and “base” of the H shell always appear at $\Delta S = 1, 0$, and -1 , respectively, independent of any model. A value of $\Delta S = 0$ corresponds exactly to a H depletion of 50% of its envelope value, while $\Delta S = 1$ and -1 correspond to H depletions of approximately 2.5% and 99.9%, respectively.

The first reaction in the CN and ON cycles, before they attain equilibrium, creates ^{13}C and ^{17}O from ^{12}C and ^{16}O , respectively. This causes the $^{12}\text{C}/^{13}\text{C}$ ratio to dip below the equilibrium value near 4, before the other reactions in the CN cycle attain equilibrium with the $^{12}\text{C}(p, \gamma)^{13}\text{N}(\beta^+ \nu)^{13}\text{C}$ reactions, thereby building up ^{12}C to its equilibrium value. This behavior can be seen in Figures 8 - 11 and indicates that one would expect to see the $^{12}\text{C}/^{13}\text{C}$ ratio decrease along the RGB beyond the start of mixing provided that the mixing extends at least into the C-depleted region on an appropriate timescale. In comparison, the $^{16}\text{O}/^{17}\text{O}$ ratio is actually much below its equilibrium value throughout most of the O-depleted zone as the ^{17}O abundance slowly enhances, then depletes near the H shell. This is presented in Figure 14 where the $^{16}\text{O}/^{17}\text{O}$ ratio is plotted for each sequence at the start of mixing and at the tip of the RGB. Due to its dependence on temperature, the $^{16}\text{O}/^{17}\text{O}$ equilibrium ratio varies depending on both the metallicity and luminosity of the model chosen. This is different from the equilibrium ratio of $^{12}\text{C}/^{13}\text{C}$ which is independent of temperature in the range relevant to these sequences.

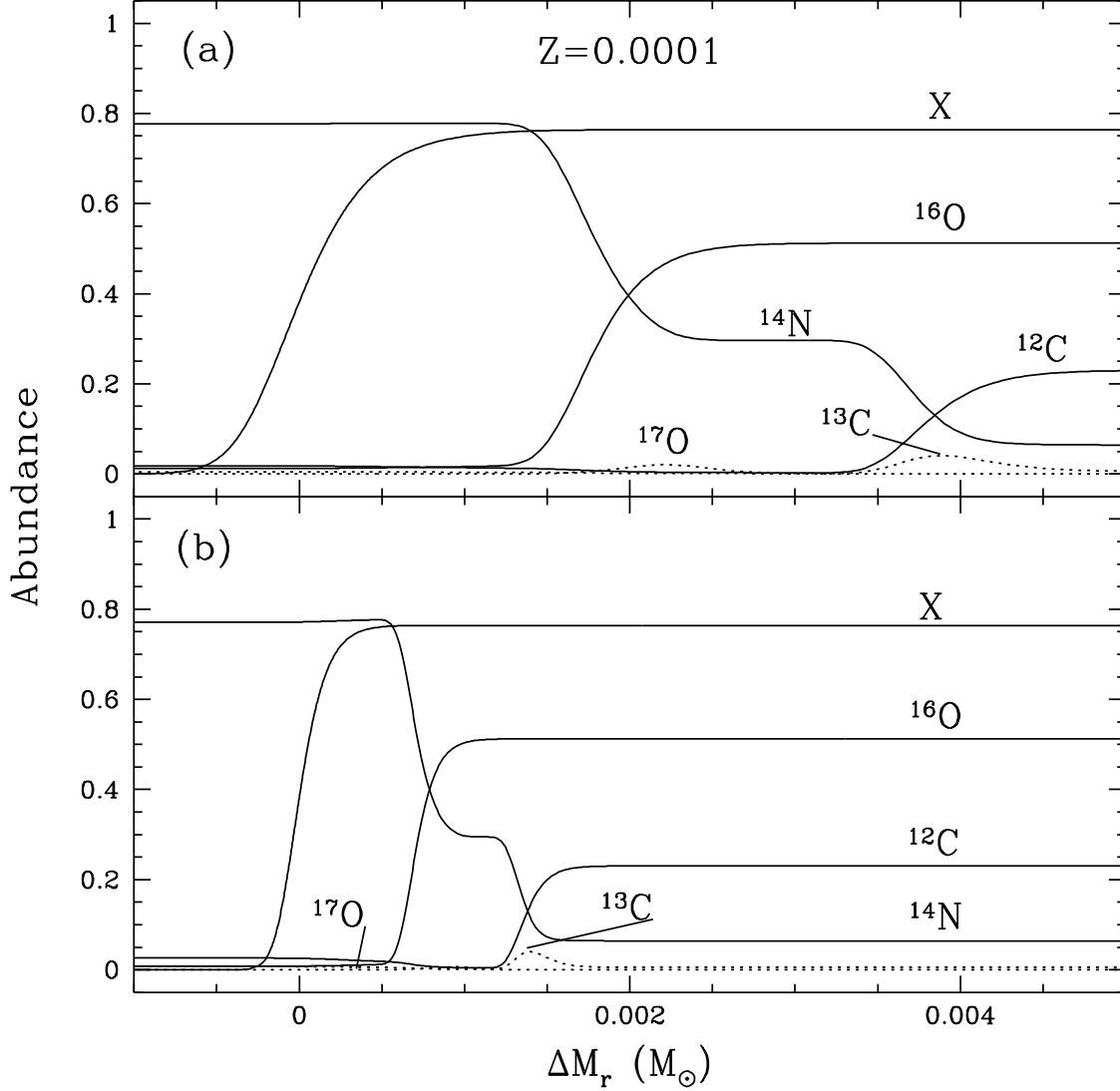


Fig. 8.— The CNO isotopic abundance profiles around the H shell (labeled by the H-mass fraction X) for the $Z = 0.0001$ sequence at (a) the presumed onset of mixing, and (b) the tip of the RGB. The ordinate is the number abundance relative to all metals. The abscissa is the mass difference, ΔM_r , between any point and the center of the H shell.

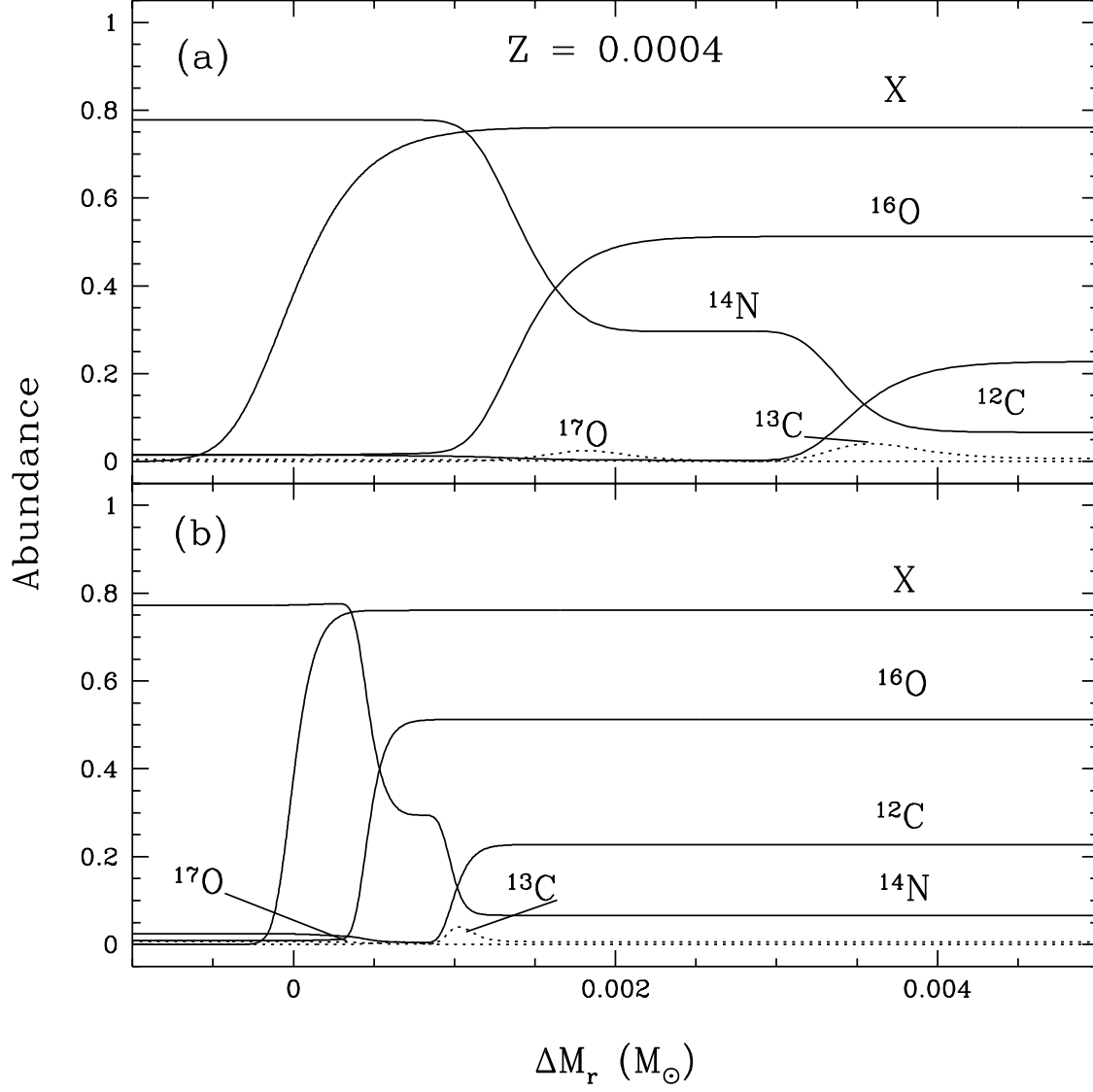


Fig. 9.— As Figure 8, except for $Z = 0.0004$.

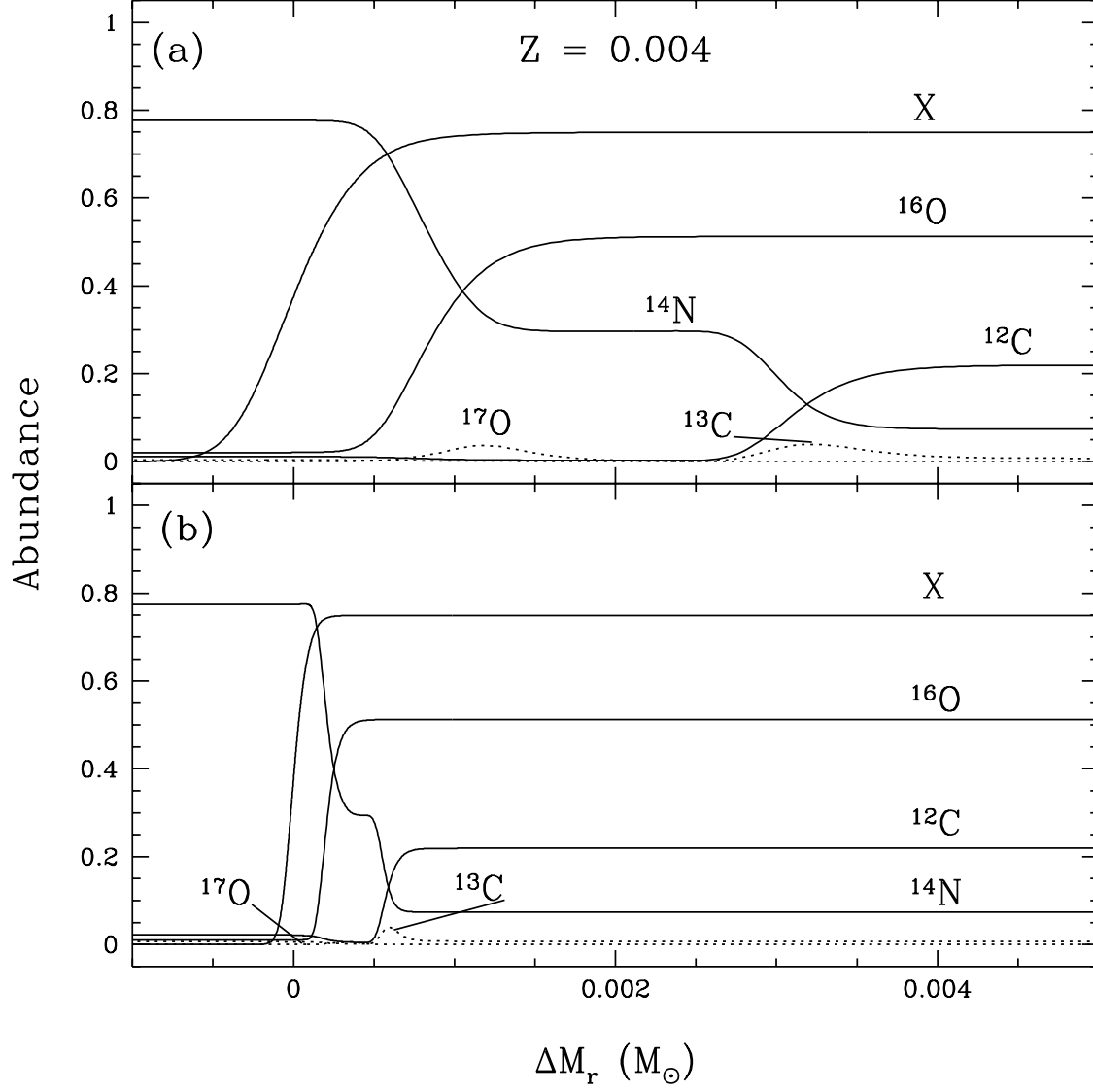


Fig. 10.— As Figure 8, except for $Z = 0.004$.

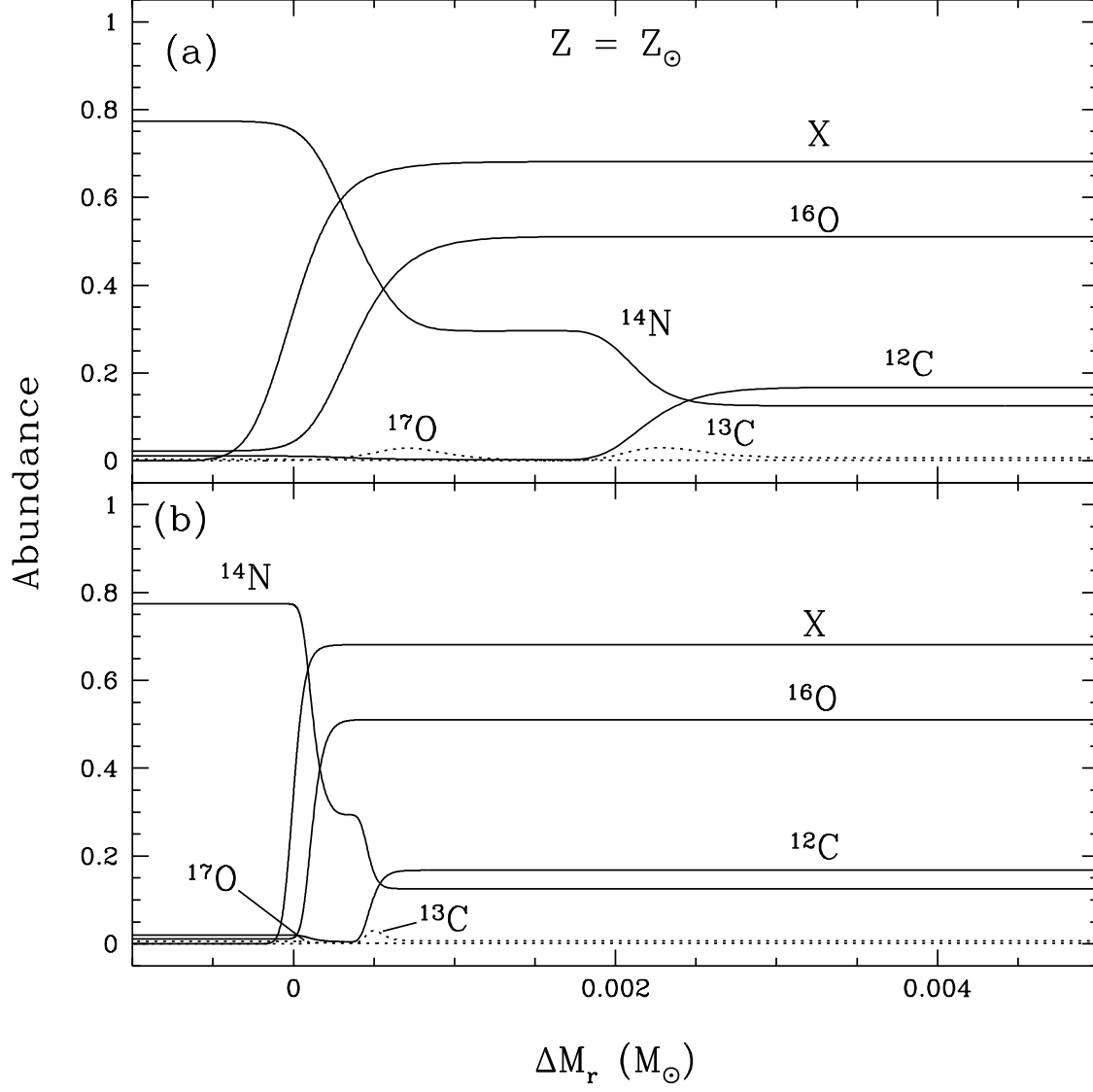


Fig. 11.— As Figure 8, except for $Z = Z_\odot$.

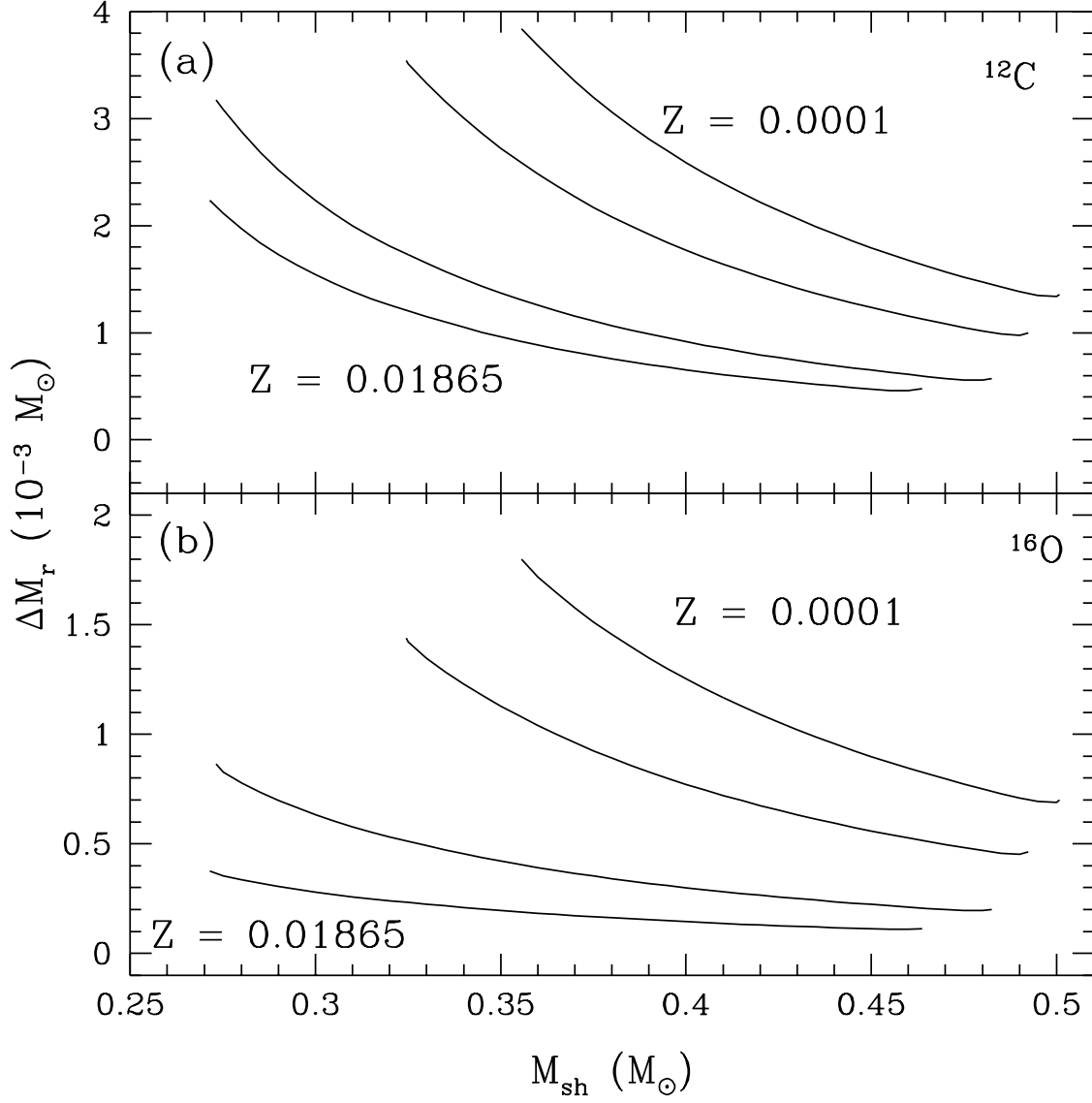


Fig. 12.— The mass difference between the center of the H shell and the point where the (a) ^{12}C and (b) ^{16}O are equal to 50% of their envelope value during the evolution of the four RGB sequences.

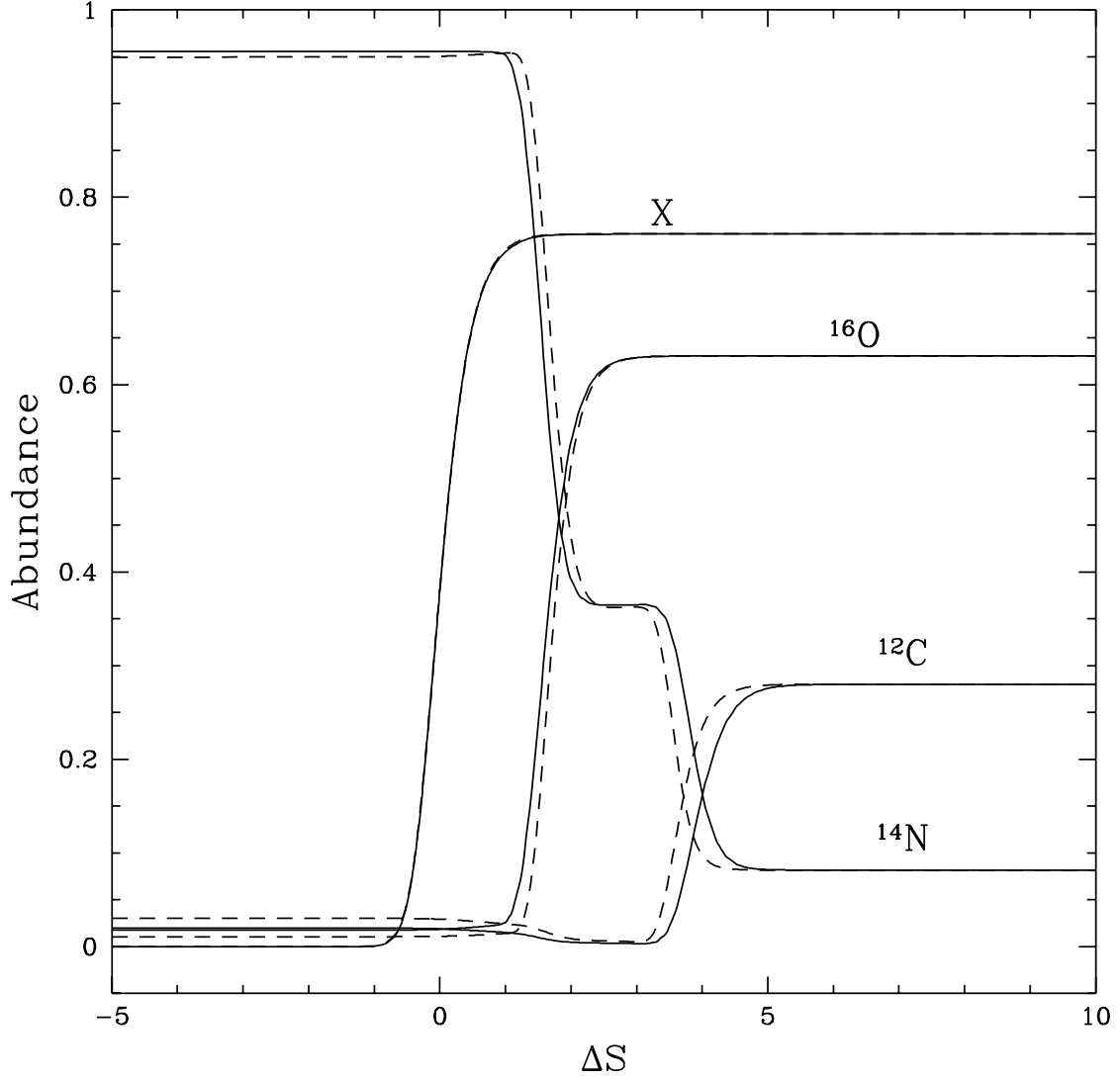


Fig. 13.— Comparison of the H and CNO profiles for the $Z = 0.0004$ sequence as a function of ΔS at the start of mixing (solid line) and at the tip of the RGB (dashed line). The hydrogen-mass fraction is traced by the curved labeled X.

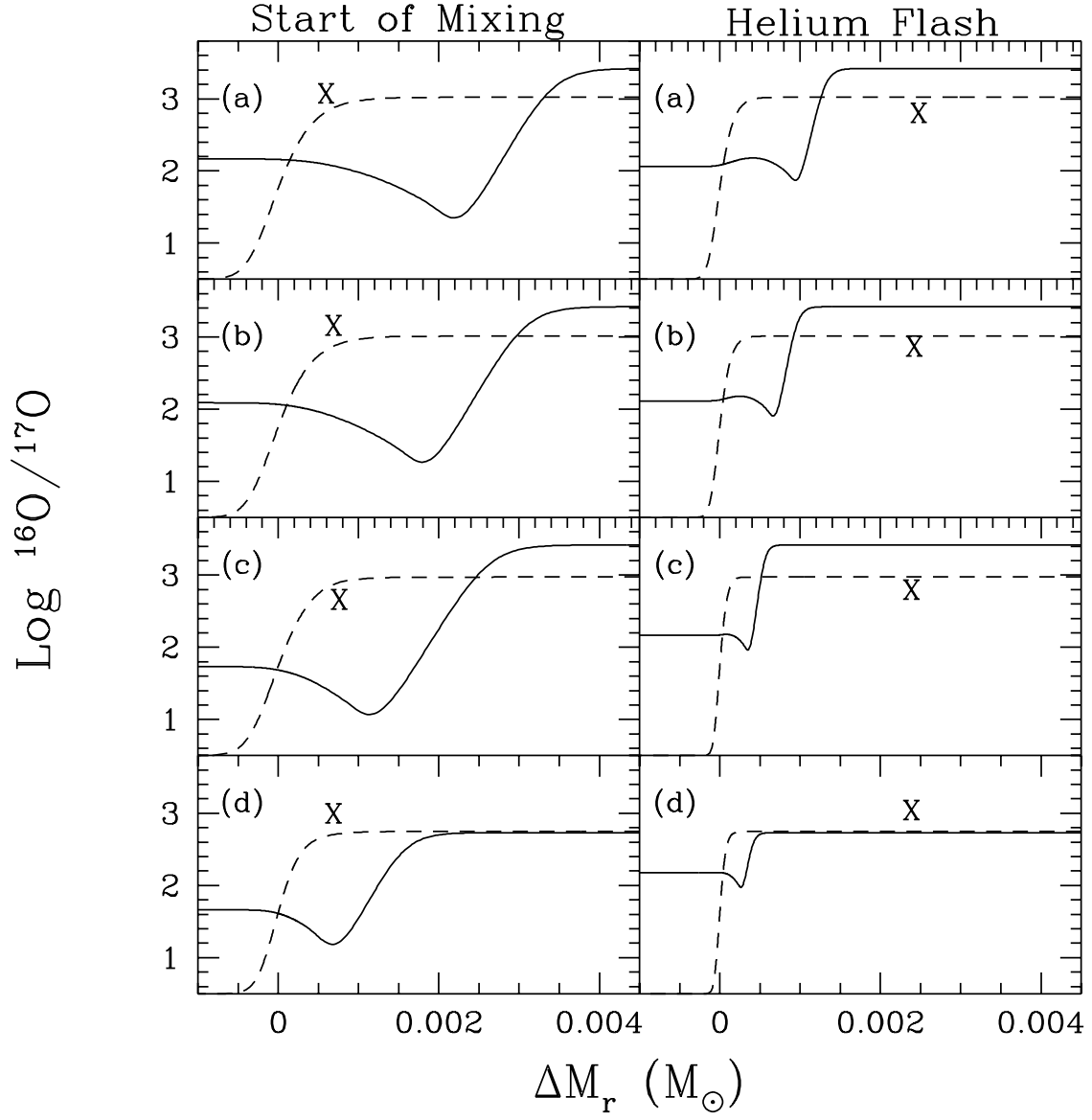


Fig. 14.— The $^{16}\text{O}/^{17}\text{O}$ ratio for the $Z =$ (a) 0.0001, (b) 0.0004, (c) 0.004, and (d) Z_\odot sequences at the start of mixing (left panels) and the tip of the RGB (right panels). The dashed curve traces the H-mass fraction, X , on an arbitrary scale.

4.2. Na-Mg-Al

We next examine the profiles of the NeNa- and MgAl-cycle isotopes, as shown in Figures 15 - 18. Because most of the processing for these two cycles occurs close to or within the H shell, we plot these figures as a function of ΔS for the sake of clarity.

The profiles for the $Z = 0.0001$ and $Z = 0.004$ sequences are slightly different from the ones presented in Paper I, since we have adjusted some of the relevant reaction rates, as discussed in section 6. All of the sequences show the initial rise in ^{23}Na from ^{22}Ne well above the H shell at the start of mixing (panel a). By the time the sequences have evolved to the helium flash (panel b), this initial Na plateau decreases in width as a result of the steepening temperature gradient. For the lowest metallicity sequence, the temperature is high enough at the onset of mixing to allow the NeNa cycle to begin building up ^{23}Na from ^{20}Ne at the top of the H shell (Figure 15a). The NeNa cycle becomes important at the start of mixing for the $Z = 0.0004$ sequence only inside the H shell ($\Delta S \sim 0.6$). In the $Z = 0.004$ sequence, this extra production of Na occurs around $\log(L/L_\odot) = 1.74$ ($M_{\text{sh}} = 0.275 M_\odot$), soon after mixing begins; but, for the $Z = Z_\odot$ sequence, ^{20}Ne never becomes a significant source of ^{23}Na compared to its production from ^{22}Ne . Figures 15b - 17b show that the NeNa cycle feeds enough ^{20}Ne into ^{23}Na to substantially increase the Na production near the tip of the RGB for all Population II metallicities, but only in the lowest metallicity RGB tip model does this occur above the top of the H shell. In the two lowest metallicity sequences, the NeNa cycle also experiences a leakage reaction through $^{23}\text{Na}(p, \gamma)^{24}\text{Mg}$ causing an enhancement in the ^{24}Mg abundance. As these two sequences evolve further up the RGB, the ^{23}Na abundance within the H shell begins to diminish as leakage from the cycle depletes the ^{20}Ne reserves. Figure 15b demonstrates this behavior. Approaching the H shell from above, the $^{20}\text{Ne}/^{23}\text{Na}$ ratio first drops below the equilibrium ratio expected from the NeNa cycle, before the $^{23}\text{Na}(p, \alpha)^{20}\text{Ne}$ reaction can build up the ^{20}Ne abundance. Around $\Delta S = 0.2$, the leakage reaction begins to drain both the ^{20}Ne and ^{23}Na , causing a local maximum at this point. Since the NeNa cycling is less robust in the higher metallicity sequences, this rise in the ^{20}Ne abundance is less apparent.

The two lowest Z sequences show that ^{27}Al enhancements at the onset of mixing come from the rapid depletions of ^{25}Mg (by way of ^{26}Al) and ^{26}Mg inside the top of the H shell (Figures 15c and 16c). On the contrary, the two highest Z sequences fail to produce any observable ^{27}Al enhancements above the center of the H shell at the onset of mixing. In fact, even at the tip of the RGB, the only Al that the $Z = 0.004$ sequence can create comes from $^{25,26}\text{Mg}$. For the $Z = Z_\odot$ sequence, ^{27}Al is only modestly produced by a minor depletion of ^{26}Mg at the tip of the RGB, while ^{25}Mg is converted into ^{26}Al at all luminosities. In this sequence, τ_{shell} is less than the decay time of ^{26}Al ($\tau = 7.4 \times 10^5 \text{ yr}$), precluding any build-up

of ^{26}Mg and ^{27}Al within or above the H shell. As the metallicity decreases, however, the total ^{27}Al increases by substantially more than can be supplied by the initial $^{25,26}\text{Mg}$. The source for this enrichment is ^{24}Mg , which is itself replenished by leakage from the NeNa cycle. By $\log(L/L_{\odot}) = 2.8$ ($M_{\text{sh}} = 0.425 M_{\odot}$), the $Z = 0.0001$ sequence begins to show the signs of enhancements in the ^{27}Al abundance from ^{24}Mg . The $Z = 0.0004$ sequence begins its “over-production” of ^{27}Al at a higher luminosity on the RGB: $\log(L/L_{\odot}) = 3.2$ ($M_{\text{sh}} = 0.475 M_{\odot}$).

The changes in the Al abundance are very sensitive to metallicity and luminosity (i.e. temperature) as shown in panels (c) and (d) of Figures 15 - 18. The reader should note that the ordinates of these panels have different scales for each sequence, with the lowest metallicity having the greatest range. For example, Figure 16d shows that for the $Z = 0.0004$ sequence, the ^{27}Al gained at the center of the H shell is +0.57 dex, which comes mostly from the decrease in $^{25,26}\text{Mg}$. In comparison, the lowest metallicity sequence shows an increase in ^{27}Al of +0.77 dex at the center of the H shell, of which only 0.42 dex comes from $^{25,26}\text{Mg}$. The other 0.35 dex is supplied by ^{24}Mg , either directly or through leakage from the NeNa cycle.

5. Consequences for Mixing

We now look at the implications of these abundance profiles if the stars were to undergo mixing. In order to fully understand the results, we must first address the question of timescales. There are several which affect the production and mixing of the elements. The first is the shell burning timescale, τ_{shell} , which allows the abundance profiles around the H shell to be set up. This is determined by the rate at which the H shell moves outward in mass and is included explicitly in our calculations through the use of the stationary shell approximation. The second is the characteristic timescale, τ_{mix} , over which the mixing carries material away from the H shell to the convective envelope. In the SM79 scenario, this is dependent upon the angular velocity and angular momentum distribution in the RGB envelope. Finally, there is the evolutionary timescale, τ_{RGB} , which determines for how long the mixing process can act and is defined by the time spent on the RGB after the H shell has burned through the H discontinuity. SM79 pointed out that the mixing process is gradual in that the timescale for changing the envelope composition does not need to be less than the shell burning timescale. If it were this rapid, there would be abrupt changes in the surface composition shortly after the onset of mixing. This is not supported by the observations. Rather, the relevant criterion is that the amount of nuclearly processed matter mixed outward from the shell over the RGB evolutionary timescale be equal to the

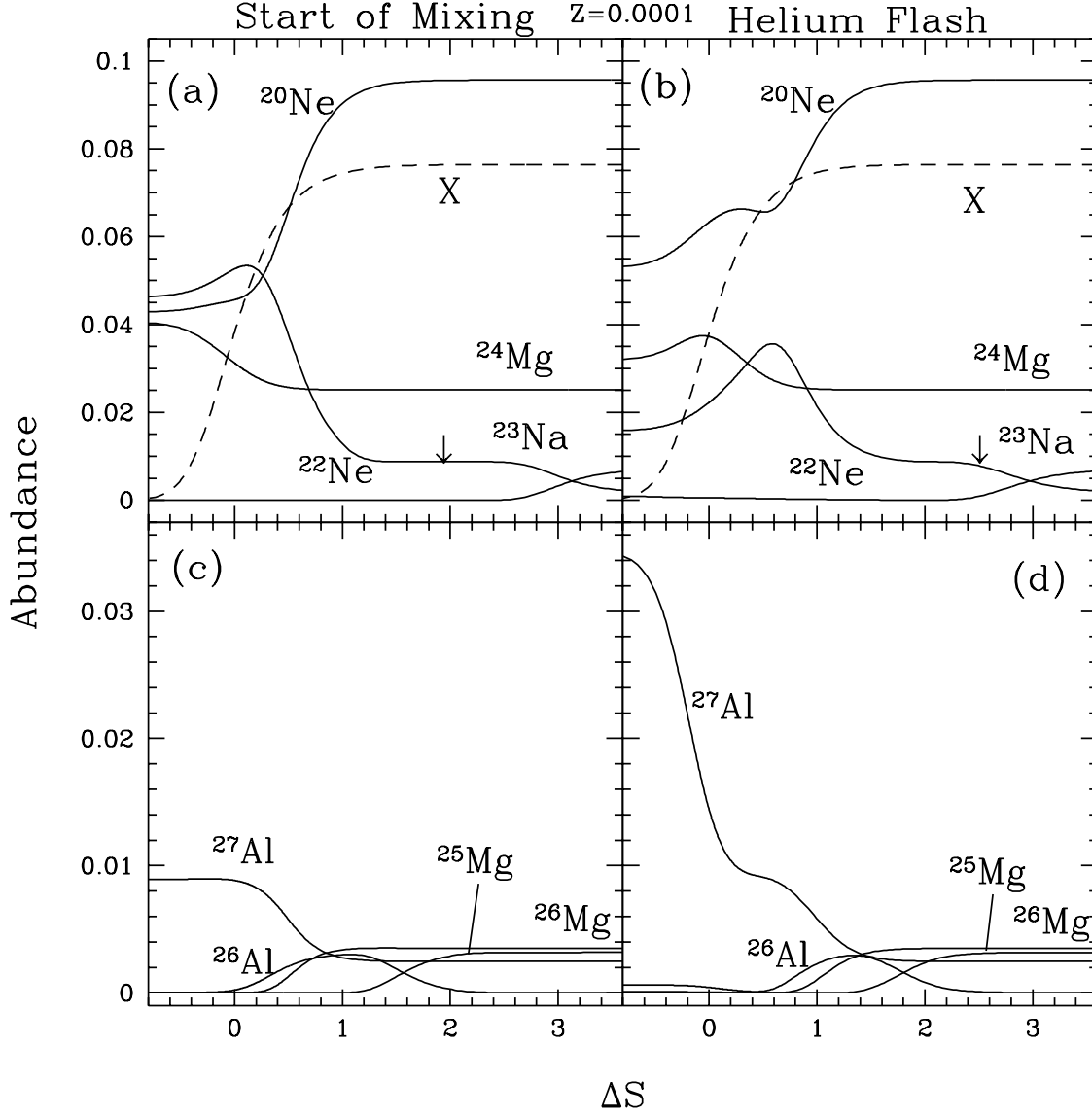


Fig. 15.— The NeNa-cycle isotopes (top panels) and MgAl-cycle isotopes (bottom panels) at the presumed start of mixing (left panels) and at the tip of the RGB (right panels) for the $Z = 0.0001$ sequence. The dashed line is the H-mass fraction scaled by a factor of 10. The ordinate is the number abundance relative to all metals. The abscissa, ΔS , is defined as the mass difference, ΔM_r , between any point and the center of the H shell divided by the H-shell thickness, ΔM_H . The arrows indicate the center of the O shell, defined as the point where the ^{16}O abundance is equal to half of its envelope value.

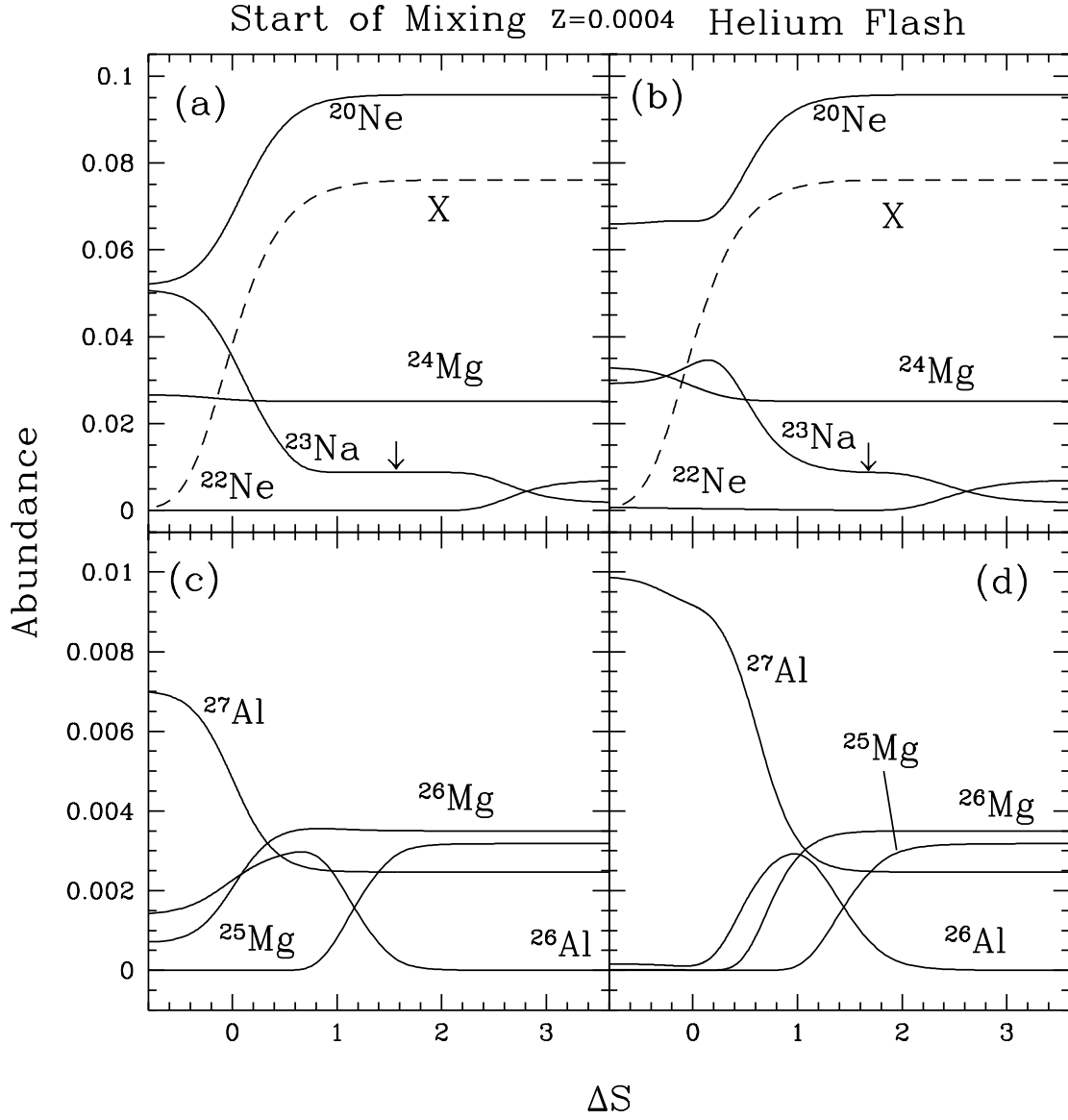


Fig. 16.— As Figure 15, but for $Z = 0.0004$.

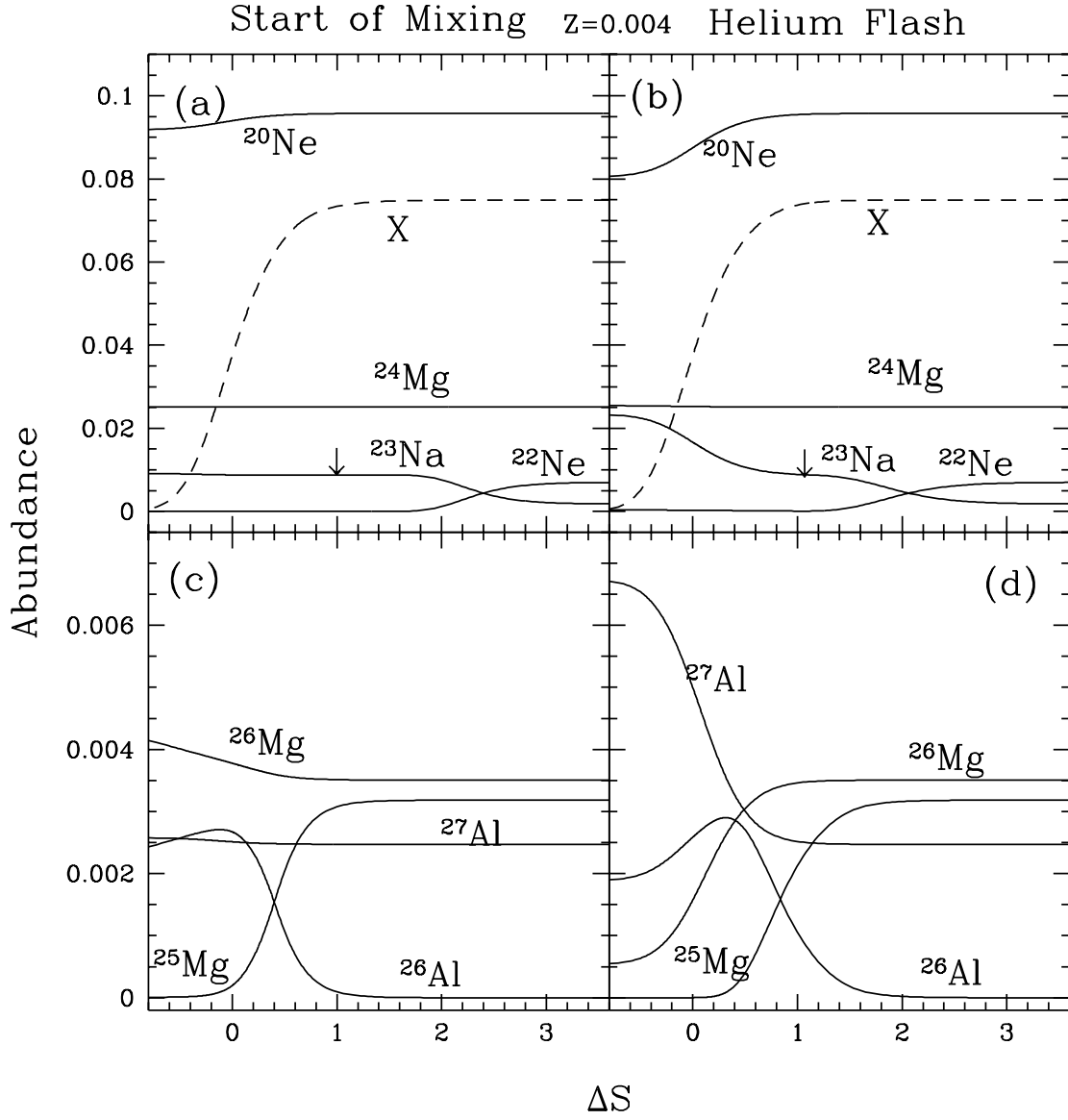


Fig. 17.— As Figure 15, but for $Z = 0.004$.

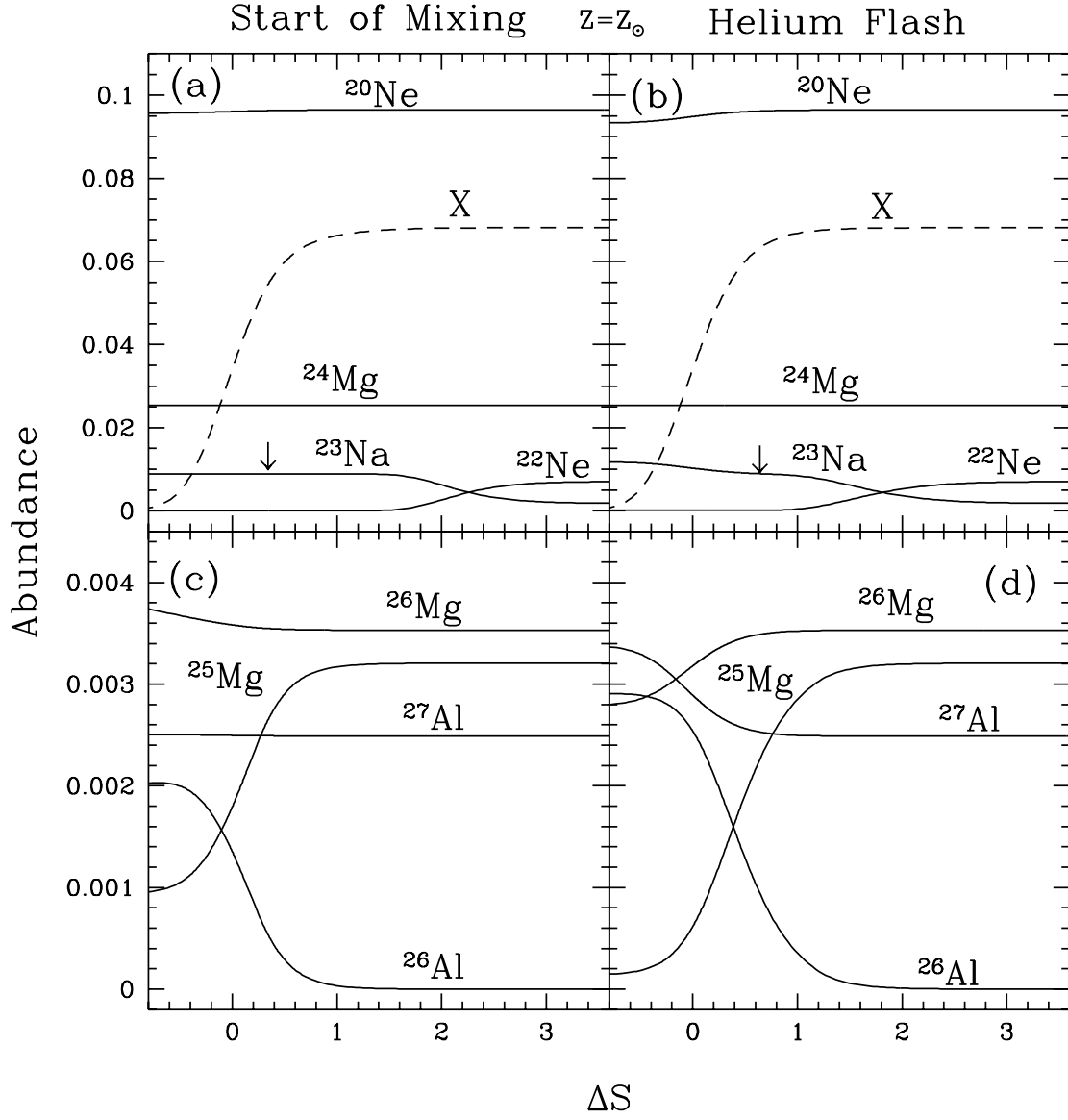


Fig. 18.— As Figure 15, but for $Z = Z_{\odot}$.

envelope mass; i.e., that most of the envelope passes through the nuclear burning regions by the time the star reaches the tip of the RGB. This is what causes the gradual changes in the abundances with increasing luminosity (see, e.g., Bell, Dickens, & Gustafsson 1979 for M92 and NGC 6397; Carbon et al. 1982 for M92; Trefzger et al. 1983 for M15; Briley et al. 1990 for NGC 6397; Briley et al. 1997 for M71).

If mixing were to occur on an appropriate timescale, what changes would we expect to see based on these sequences? The answer, of course, depends on the depth of mixing. For example, all of the sequences behave similarly regarding the CNO abundances. The distinguishing characteristic which separates one sequence from another is the distance above the H shell of the C- and O-depletion regions as discussed in section 4.1, and shown in Figures 8 - 11. Thus, we anticipate that there would be C vs. N and O vs. N anticorrelations at all metallicities, with the extent of their variations depending on the depth of mixing. Along with these anticorrelations, we would expect to see the $^{12}\text{C}/^{13}\text{C}$ ratio near its equilibrium value of 4 if mixing penetrated far enough into the C-depleted region to cause a C vs. N anticorrelation. Likewise, if mixing reached deeply enough to cause an O vs. N anticorrelation, we would expect to see the $^{16}\text{O}/^{17}\text{O}$ ratio near its equilibrium value between ~ 50 and 150, depending on the metallicity and luminosity of the model. The observations show C vs. N anticorrelations and $^{12}\text{C}/^{13}\text{C}$ ratios near equilibrium in clusters of all metallicities (see, e.g., Norris 1981; Smith & Norris 1983; Smith & Bell 1986; Pilachowski 1988; Briley et al. 1989; Smith & Mateo 1990; Sneden et al. 1991; Smith et al. 1996; Smith et al. 1997), but there is less evidence of O vs. N anticorrelations in the more metal-rich clusters (Dickens et al. 1991; Sneden et al. 1994; Briley, Smith, & Lambert 1994; Norris & Da Costa 1995a; Briley et al. 1997). There is yet no data available for the $^{16}\text{O}/^{17}\text{O}$ ratio in globular cluster stars. This constrains both τ_{mix} and the depth of mixing for the higher metallicity clusters. Perhaps the trends seen in the higher metallicity clusters are the result of narrower shell processing regions which allow less material to be synthesized in a given time. In any case, the metallicity at which the results of the O-N conversion become commonplace seems to be between the $Z = 0.0004$ sequence (for example, M13 [KSLS93]) and the $Z = 0.004$ sequence (M71 [Sneden et al. 1994; Shetrone 1996a]).

Understanding the implications of the Na, Mg, and Al isotopic abundances is complicated by the fact that their yields are very sensitive to the sequence metallicity and model luminosity. In fact, the only similarity among the sequences is the production of ^{23}Na from ^{22}Ne in a plateau region above the H shell. This region becomes more narrow and moves closer to the H shell with both increasing luminosity and metallicity. Figures 15 - 18 show the initial change in the Na abundance relative to the center of the O shell, which we define as the point where the ^{16}O abundance is equal to half of its envelope value,

and mark with an arrow above the ^{23}Na curve. The reader may notice that when shown in ΔS -space, the center of the O shell actually moves *away* from the center of the H shell with increasing luminosity, indicating that the H shell is steepening more quickly than the O-depleted region is narrowing. At lower luminosities the Na is enhanced above the center of the O shell. This leads to a scenario where Na can be increased without altering the O abundance as observed in the metal-poor stars of ω Cen by Norris & Da Costa (1995a) and in the metal-rich cluster NGC 362 by Briley et al. (1997). As the sequences evolve, the Na-enriched region overlaps the O-depleted region and helps to describe the global anticorrelation between O and Na (Norris & Da Costa 1995b; Kraft et al. 1997). The ^{23}Na abundance becomes more strongly enhanced as the result of the NeNa cycle only in the two most metal-poor sequences and only within or very close to the H shell. To reach this abundant supply of Na would require mixing deeply into the O-depleted region, implying that large Na enhancements should be accompanied by large O depletions, as seen in M13 (Kraft et al. 1997)

For the other isotopes in the NeNa and MgAl cycles, it is instructive to look at a comparison of two sequences at a common luminosity in order to gain some insight into how the metallicity affects the interpretation of the models. In Figure 19, we plot the NeNa (panel a) and MgAl (panel b) isotopes for the two metallicities which represent the extremes in our sequences. Clearly there is much more processing occurring in the low metallicity sequence where the temperatures are higher. The high metallicity sequence shows less robust processing: ^{23}Na is slightly enhanced from ^{22}Ne and Al is increased mostly in the form of the meta-stable isotope of ^{26}Al which decays to ^{26}Mg . Thus, deep mixing in the metal-richest sequence would produce little changes in these elements unless the ^{26}Al could be mixed to the surface in large quantities before decaying. If τ_{mix} is longer than the ^{26}Al half-life, then the $^{26}\text{Mg}/^{25}\text{Mg}$ ratio would be seen to increase in a metal-rich, deep mixing scenario. As the metallicity decreases, the ^{27}Al does begin to build up from both $^{25,26}\text{Mg}$ (see, e.g., Figure 17d) due to the increasing temperatures. The metal-poor sequences are able to produce more ^{27}Al than can be accounted for by $^{25,26}\text{Mg}$, as demonstrated by Figure 19b. The extra Al enhancements occur on the upper RGB at the base of the H shell. Therefore, in order for the depletion of Mg and the large Al enhancements to be seen at the stellar surface, mixing must occur deep within the H shell during the latter half of the RGB lifetime. The corollary to this is that if large Al enhancements are seen, they should be accompanied by large increases in N and Na, and large decreases in $^{25,26}\text{Mg}$ and ^{16}O . (We discuss the effect on ^{24}Mg later.) Since the changes occur only on the upper RGB, there are now tighter constraints on the mixing time.

Our results are qualitatively consistent with the relatively few observations of total Mg abundances. That is, deep in the H shell where there are large Al enhancements, the total

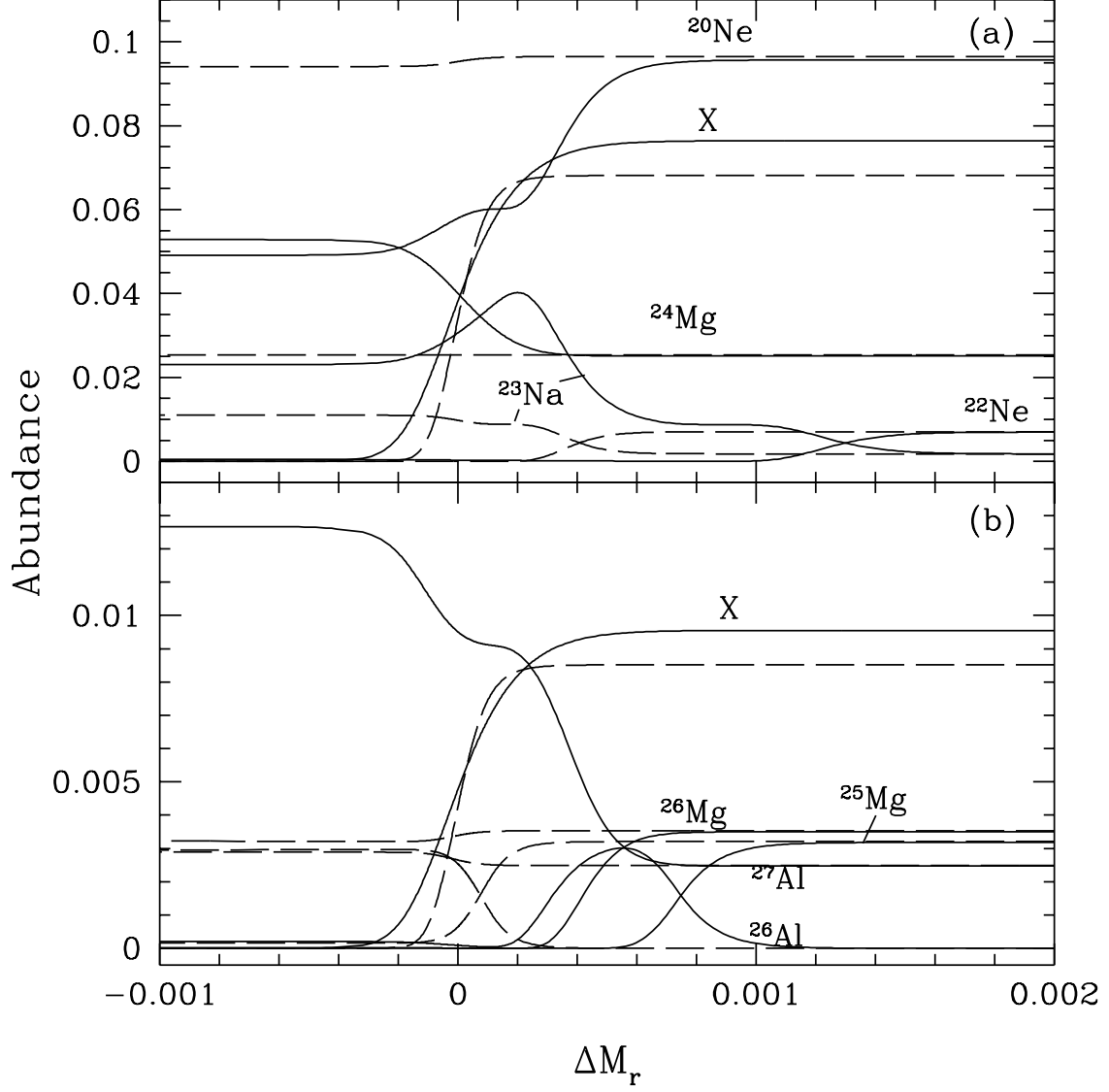


Fig. 19.— (a) The NeNa cycle isotopes for the $Z = 0.0001$ (solid line) and $Z = Z_\odot$ (dashed line) sequences at $\log(L/L_\odot) = 3.0$. (b) The MgAl cycle abundances for the same models in panel (a). The hydrogen-mass fraction, X , is scaled by a factor of 10 in panel (a), and by a factor of 80 in panel (b).

Mg abundance is depleted, in accord with the observations of M13 RGB tip giants as seen by Shetrone (1996b), PSKL96, and Kraft et al. (1997). This is in spite of the leakage from the NeNa cycle which creates a surplus of ^{24}Mg . For example, at the tip of the RGB in the $Z = 0.0004$ sequence, the total Mg abundance at the center of the H shell decreases by 9.9% relative to the envelope value, while the ^{24}Mg abundance increases by 14%. Only if mixing were to penetrate more deeply than this would the total Mg abundance become enhanced.

On the other hand, our models are at odds with the observations of the Mg isotopes in M13 and NGC 6752 by Shetrone (1996b, 1997). Whereas he observes a decrease in ^{24}Mg which anticorrelates with Al, we predict an increase in ^{24}Mg as previously noted. This increase, of course, is dependent on the accuracy of the $^{23}\text{Na}(p, \gamma)^{24}\text{Mg}$ rate as discussed in section 6.2. In addition, the Shetrone results show a low abundance of both $^{25,26}\text{Mg}$ when Al is low, and an increased abundance when Al is enhanced. This is difficult to explain given our present understanding of the nuclear reaction rates. We show that when Al is slightly enhanced, as in the star L598 in M13, the isotopes which create the Al are $^{25,26}\text{Mg}$. However, when Al is substantially increased ($\Delta\text{Al} \sim +1.0$ dex), we predict that ^{24}Mg is the source of that enhancements *and* that both $^{25,26}\text{Mg}$ remain depleted. The Shetrone observations show that ^{24}Mg is indeed the source of the large Al enhancements, but they also show that the other two isotopes are somehow increased. Since, the ^{24}Mg proton-capture rate is much slower than either the ^{25}Mg or ^{26}Mg rates at the canonical temperatures in the H shell, any ^{24}Mg depletions should be accompanied by a permanent diminution of $^{25,26}\text{Mg}$.

$^{25,26}\text{Mg}$ become important at lower temperatures. ^{25}Mg is easily converted into ^{26}Al in all sequences. Only in the lower luminosity Population I models is it not completely exhausted. Decreasing the metallicity of a sequence extends τ_{shell} and allows the resultant ^{26}Al to decay into ^{26}Mg before the shell overtakes the abundance profiles, as in the higher metallicity sequences. ^{26}Mg , on the other hand, requires higher temperatures before it can be processed into ^{27}Al . These last two points explain why ^{26}Mg is seen to increase below the H shell in the solar-metallicity sequence. The implications for the two Mg isotopes is that one should expect to see an anticorrelation between $^{25,26}\text{Mg}$ and $^{26,27}\text{Al}$ which becomes more pronounced at lower metallicities and higher luminosities. Whether this can be seen in the higher metallicity sequences is also a matter of how much mixing can occur in these stars and is the subject of future work.

Finally, we look at the effect of all three Mg isotopes in the context of recent observations, which might be explained in the following manner. For stars on the lower RGB or with high metallicity where the temperatures are too low to process ^{24}Mg and ^{23}Na , the Al abundance is dominated by the destruction of $^{25,26}\text{Mg}$. In these stars we expect to see an anticorrelation between the total Mg and Al abundances. Because the heavier two

Mg isotopes are depleted in the region of large Na production and O depletion, this would produce an anticorrelation between Na and Mg and a correlation between O and Mg as well, as seen by PSKL96. However, since the Na is initially increased in the ^{22}Ne -burning plateau above the region of Mg depletion, it should not be surprising to see some increase in Na before seeing a change in Mg. Whether or not the spread in the Mg abundance is correlated with the small increases in Na depends on the depth of mixing. For metal-poor RGB tip stars, where the NeNa cycle begins leaking strongly into the MgAl cycle, we expect both the Al and Mg abundances to be controlled by ^{24}Mg after the initial $^{25,26}\text{Mg}$ has been depleted. According to the nuclear reaction rates we have used, these stars would exhibit a ^{24}Mg -Al correlation and either a Mg-Al correlation or anticorrelation, depending on the depth of mixing. We discuss possible remedies for the discrepancies between our results and the observations in section 6.

One test of the significance of leakage into the MgAl cycle can be achieved by checking the constancy of $[(\text{Mg}+\text{Al})/\text{M}]$ among the cluster stars². Any leakage would cause this quantity to show star-to-star variations. Shetrone (1996a) has shown that the stars in M13 conserve the total number of Mg and Al nuclei. However, this hypothesis is difficult to test since, as we show in Figure 20, the total variation in the number of MgAl cycle nuclei due to leakage is only 0.045 dex at the center of the H shell at the tip of the sequence which represents the metallicity of M13, and is much less at lower luminosities. A variation of this magnitude is typically much less than the uncertainties in the abundance measurements, and therefore, not likely to be observed.

6. Nuclear Reaction Rate Uncertainties

Our nuclear burning code includes some changes to reflect modern results for the nuclear reactions involved in the CNO, NeNa, and MgAl cycles. In this section we explore the uncertainties in the reactions used in the code and discuss their effect on our results.

6.1. ^{17}O Proton Captures

In the ON cycle, we substituted updated rates for the $^{17}\text{O}(p, \alpha)^{14}\text{N}$ and $^{17}\text{O}(p, \gamma)^{18}\text{F}$ reactions based on the formulae from Landré et al. (1990). These rates are based on indirect measurements of the proton width of the resonant state at 66 keV. The formulae include

²In this instance, we use M to refer to the number abundance of metals.

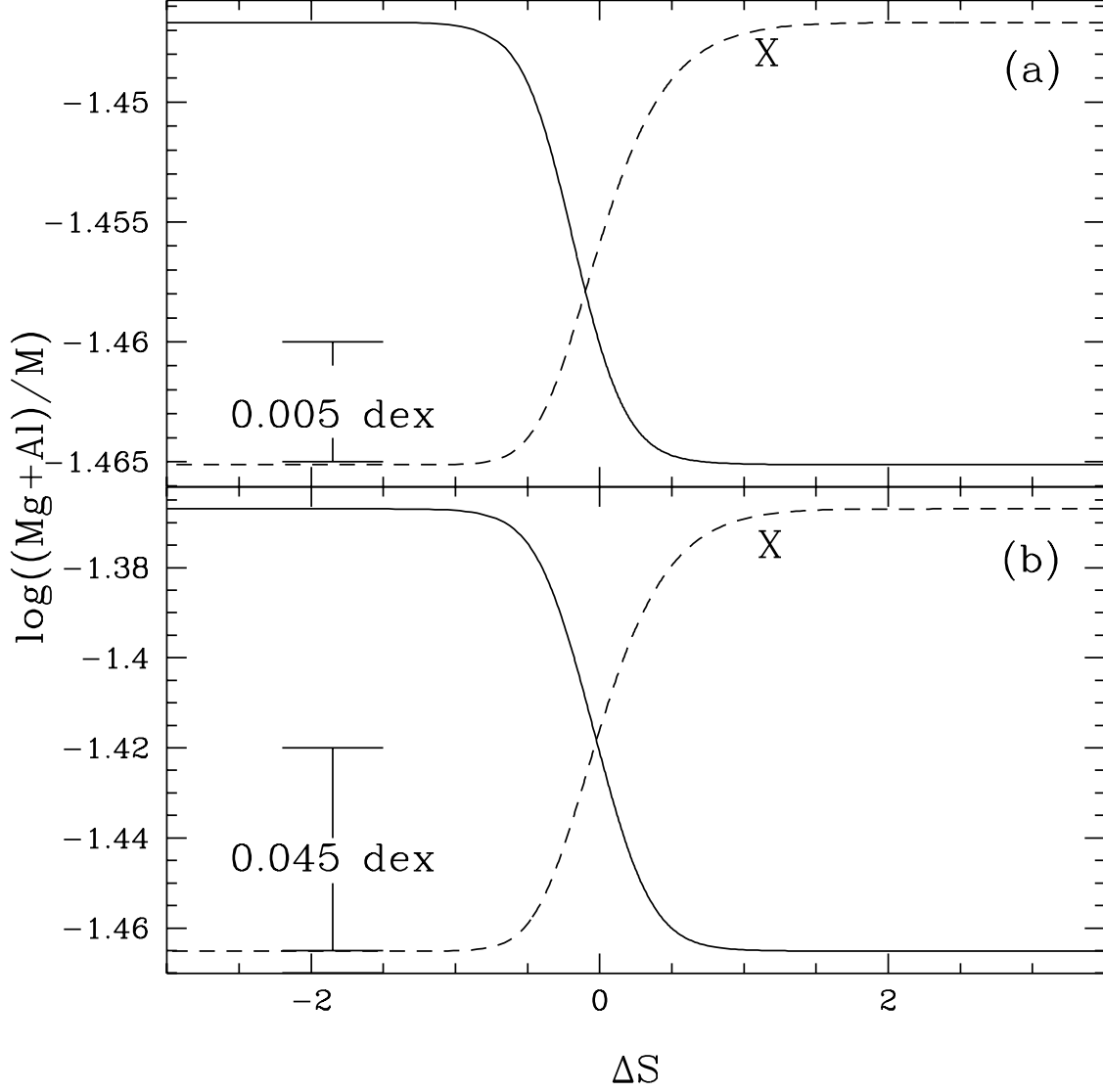


Fig. 20.— The variation in the total Mg+Al nuclei due to leakage from the NeNa cycle for the $Z = 0.0004$ sequences at (a) the onset of mixing (b) the tip of the RGB.

two factors, f_1 and f_2 , that reflect the range of error in the measurement of the resonance at 66 keV and a higher level resonance in ^{18}F , respectively. For each decay channel f_1 is given a value between 0.2 and 1, and f_2 a value between 0 and 1. Blackmon et al. (1995) have since directly measured the cross section at energies near the 66 keV resonance of $^{17}\text{O}(p, \alpha)^{14}\text{N}$ and concluded that the total reaction proceeds at approximately 10 times the rate given by CF88. Therefore, we used the formulae given by Landré et al. (1990), but we extended f_1 down to a value of 0.05 to allow the alpha-decay reaction rate to fall in line with the direct measurements of Blackmon et al. (1995). Since the resonance at 66 keV dominates both rates for $0.01 < T_9 < 0.07$, the value of f_2 is inconsequential; as such, we adopted $f_2 = 0.1$. Figure 21 compares the cross-sections of Landré et al. (1990), using two values of f_1 , with the rates of CF88. The dashed lines represent the value of 0.3 chosen in Paper I, while the dotted lines show the cross-sections used in this work. It is clear from panel (a) that our rate for the $^{17}\text{O}(p, \alpha)^{14}\text{N}$ reaction is around ten times that of CF88. Since there are no new data for the $^{17}\text{O}(p, \gamma)^{18}\text{F}$ reaction rate, we use the same values for f_1 and f_2 as in the α -decay rate and determine that this new rate agrees fairly well with that of CF88, as shown in Figure 21b. The most significant impact of the former rate is on the $^{16}\text{O}/^{17}\text{O}$ equilibrium ratio. Using the presently modified rates of Landré et al. (1990) yields a temperature-dependent ratio between 50 and 150 in the range $0.03 \lesssim T_9 \lesssim 0.06$ with a peak near $T_9 = 0.045$. This is at least a factor of ten larger than predicted with the rates of CF88.

6.2. NeNa Cycle Reactions

We have replaced the rates of CF88 in the NeNa cycle by those of El Eid & Champagne (1995; hereafter, EC95). As done by CF88, EC95 modified some terms in their rates by a factor which ranges from 0 to 1 to reflect the uncertainty in some resonances. Following the lead of CF88, we use an intermediate value of 0.1 for all such terms and check the effect of doing so on our analysis. The rate of the first reaction in the cycle, $^{20}\text{Ne}(p, \gamma)^{21}\text{Na}$, is very well determined. This reaction is followed by a β^+ -decay, which is very rapid compared to the reactions in the cycle, as are most of the decays in both the NeNa and MgAl cycles. The next reaction in the cycle is $^{21}\text{Ne}(p, \gamma)^{22}\text{Na}$. Since there is no appreciable source of ^{21}Ne before the cycle starts and since this reaction is faster than the ^{20}Ne proton capture by orders of magnitude at the H-shell temperatures, any uncertainty in its rate is inconsequential to the production of ^{23}Na . On the contrary, while $^{22}\text{Ne}(p, \gamma)^{23}\text{Na}$ proceeds much more rapidly than the ^{20}Ne proton capture, there is an appreciable source of ^{22}Ne in the envelope; therefore, it is important to understand this rate well, particularly in the higher metallicity sequences where the Na production might be dominated by ^{22}Ne . As

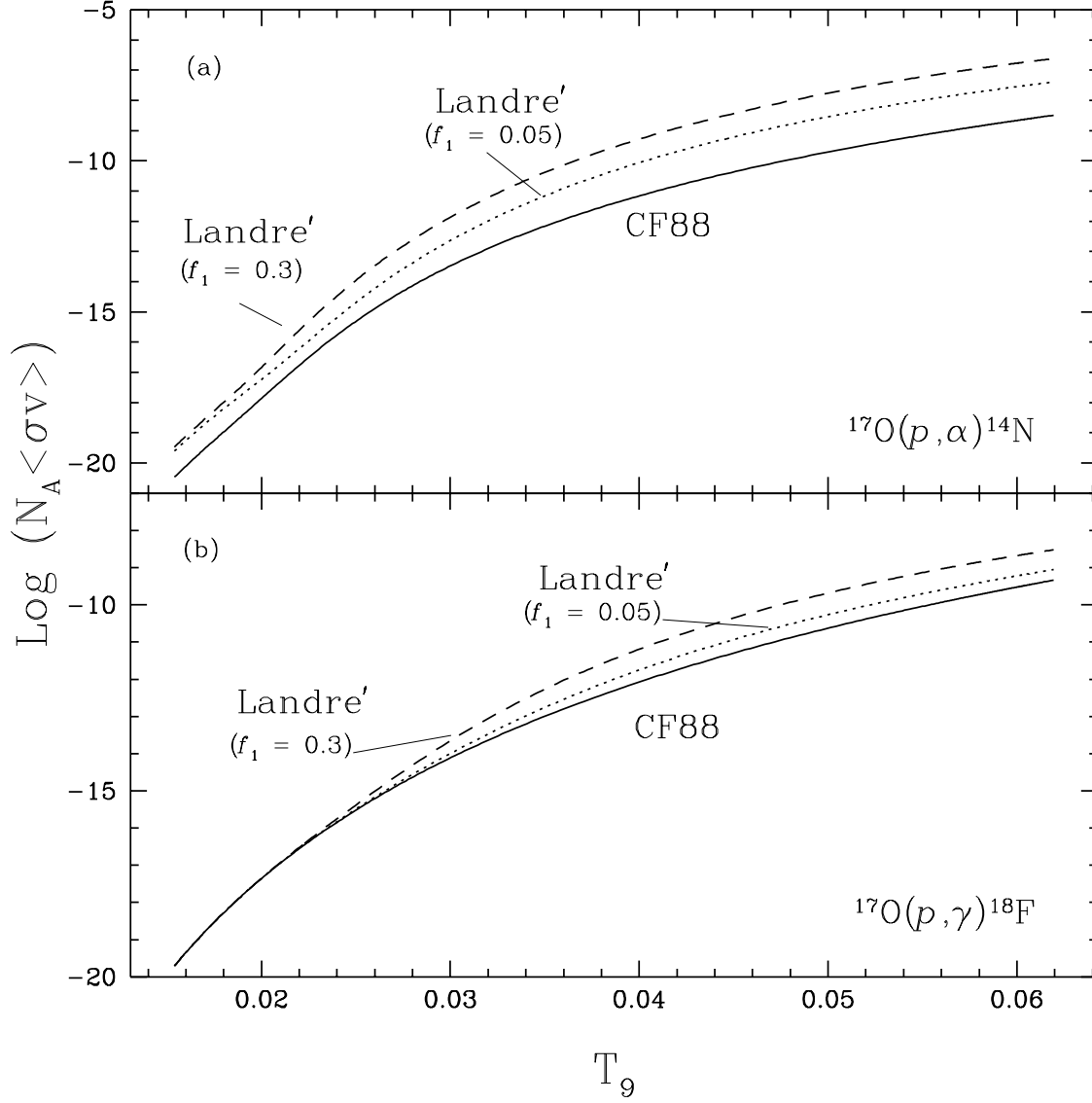


Fig. 21.— A comparison of the new O proton-capture rates from Landré et al. (1990) with those of CF88 for two values of f_I . The ordinate is in logarithmic units of $\text{cm}^3 \text{s}^{-1} \text{mole}^{-1}$.

discussed in EC95, the increase of the lowest resonance by 6 keV to 36 keV causes the lower limit for this rate to be 5-30 times faster than the CF88 rate in the range $T_9 = 0.02-0.05$. This is the reason why the Na plateau exists so much further above the center of the O shell than originally suggested by the CF88 rates: the EC95 ^{22}Ne proton-capture rate proceeds nearly a factor of 40 faster than $^{16}\text{O}(p, \gamma)^{17}\text{F}$ at $T_9 = 0.035$, as opposed to nearly a factor of unity with the CF88 rates. In addition, two resonances near 68 keV and 100 keV can cause this rate to be as much as a factor of two higher at $T_9 = 0.03$ than the suggested lower limit that we have used in the code. Using the upper limits to this rate produces a broader Na plateau that extends a factor of two further above the O-depleted region than when using the lower limits. Mixing into this region can create large Na enhancements without affecting the O abundance. This could further explain the results of Norris & Da Costa (1995a) and Briley et al. (1997).

The most important rates to understand in the NeNa cycle for determining the Na and Mg abundances at lower metallicities are the cycling reaction, $^{23}\text{Na}(p, \alpha)^{20}\text{Ne}$, and the leakage reaction, $^{23}\text{Na}(p, \gamma)^{24}\text{Mg}$. The former reaction contains an upper limit on the 36 keV resonance, which can become important for lower temperatures around $T_9 = 0.04$. At temperatures higher than this, the contribution quickly becomes insignificant when compared to the other well-known terms. The leakage reaction has an uncertain resonance near 137 keV which becomes important only near $T_9 = 0.07$, which is never attained in our models, even near the tip of the RGB. Using these rates, we determine the ratio of leakage to cycling, R_{lc} , and compare it with the same ratio from CF88. The results are given in Figure 22, where the curve represents the ratio of the rates given by EC95 over the ratio of the rates given by CF88. At low temperatures, R_{lc} is nearly 55 times stronger with the new rates, but only 4-6 times stronger in the important temperature range, $0.04 \leq T_9 \leq 0.06$. Varying the values of the uncertain terms, from their least to highest possible contributions, in all combinations has the effect of introducing a factor of 10 uncertainty in R_{lc} at $T_9 = 0.03$. For $T_9 = 0.05$, the total range in uncertainty is only $\pm 1\%$. Although the comparative leakage rate can be much faster at lower temperatures, the absolute rate for the $^{23}\text{Na}(p, \gamma)^{24}\text{Mg}$ reaction is still about 5 orders of magnitude less at $T_9 = 0.03$ than at $T_9 = 0.05$. Therefore, the uncertainty in the leakage at lower temperatures has an insignificant effect on the final abundances. Finally, from Figure 22, it is apparent that the eventual production of ^{27}Al through the connection between the NeNa and MgAl cycles at the shell temperatures becomes more likely with the rates of EC95.

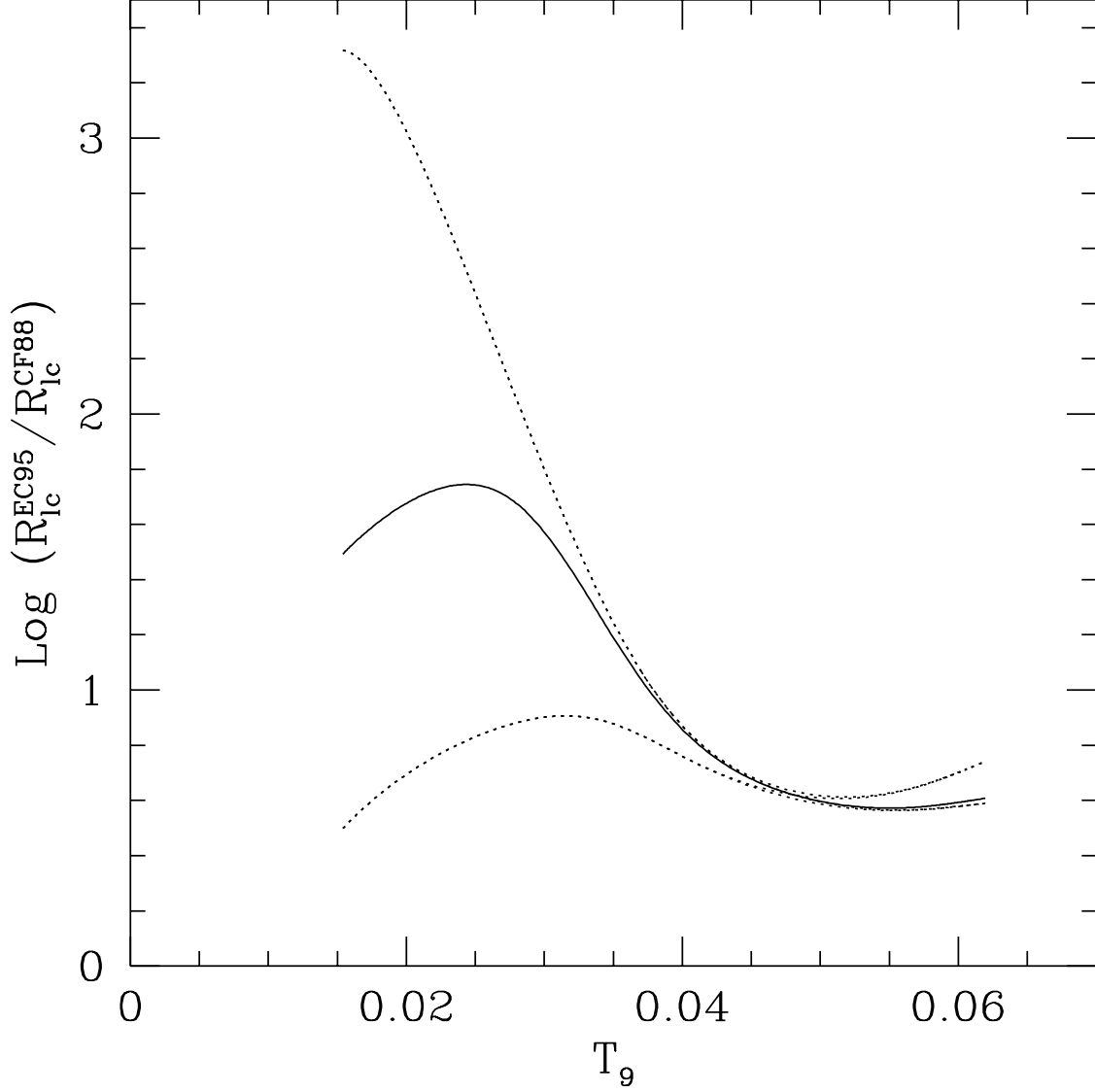


Fig. 22.— The ratio of the “leakage-to-cycling” ratios (R_{lc}) of the EC95 and CF88 rates. The graph is read, for example, by saying that at $T_9 = 0.035$, the EC95 rates predict 10 times as much leakage from the NeNa cycle as the CF88 rates. The dotted lines represent the published uncertainties in the EC95 rates, while the solid lines represents the EC95 rates used in this work.

6.3. MgAl Cycle Reactions

In this section we explore how the changes in the reaction rates of the MgAl cycle might affect the abundances of Mg and Al in general, and ^{24}Mg in particular. In order to match Shetrone’s observations of M13 giants, the abundance of ^{24}Mg must somehow be reduced, at least near the tip of the RGB. To begin we explore how changes in the proton-capture rates of ^{23}Na , $^{25,26}\text{Mg}$, and ^{27}Al might affect the production and destruction of ^{24}Mg . One method which might accomplish this is to slow the rate of leakage from the NeNa cycle. Figure 23 shows the rate of destruction of ^{24}Mg compared to its rate of production from ^{23}Na and ^{27}Al in the $Z = 0.0001$ helium-flash model, which has the largest range in temperature (see Figure 9). The new rates for the $^{27}\text{Al}(p, \alpha)^{24}\text{Mg}$ reaction are from Iliadis (private communication; see below). One curve shows the destruction-to-production ratio for the CF88 rates and two show the same for the upper and lower limits of the EC95 rates. Since this is done for an actual model, the number of available reactant nuclei is taken into account. If we compared the production rates of ^{24}Mg only from the ^{23}Na proton captures and ignored its production from $^{27}\text{Al}(p, \alpha)^{24}\text{Mg}$, then the CF88 curve would be nearly a factor of 6 greater than the EC95 curves; however, because the α -decay reaction from ^{27}Al is more rapid with the CF88 rates than with the newer Iliadis rates, all three ratios are similar. Above the H shell, where the destruction-to-production ratio is less than unity, it is apparent that the range in uncertainty due to the EC95 rates cannot weaken the leakage from the NeNa cycle enough to allow the destruction rate of ^{24}Mg to overcome its production rate.

Now let us put aside the quoted uncertainties from EC95 and explore some other nuclear-physics limits. We begin by completely shutting off the NeNa-cycle leakage. This will allow the ^{24}Mg to deplete with only marginal production from $^{27}\text{Al}(p, \alpha)^{24}\text{Mg}$ at higher temperatures. Figure 24 shows Mg plotted against Al for both leakage via the EC95 rates and no leakage, for the $Z = 0.0004$ sequence at the RGB tip. The initial anticorrelation at low Al/M is due to depletions in $^{25,26}\text{Mg}$. We see from this figure that with NeNa-cycle leakage occurring, the ^{24}Mg abundance increases at high Al causing the upturn in the Mg/M abundance. On the contrary, once the leakage is shut off, the total Mg abundance diminishes, resulting in a total change of ~ -0.1 dex in Mg and $+0.6$ dex in Al. According to Figure 6 in Shetrone (1996b), the total Mg depletes by ~ 0.4 dex while the Al increases by ~ 1 dex. Clearly, limiting the leakage from the NeNa cycle alone is not enough to account for the observations. In addition, the extra-depletion of ^{24}Mg with the leakage shut off might occur too deep within the H shell to be mixed outward.

The ^{25}Mg proton captures are from Iliadis et al. (1996) and are well-determined in the range of T_9 from 0.01 to 0.06, with the largest uncertainty being less than a factor of two

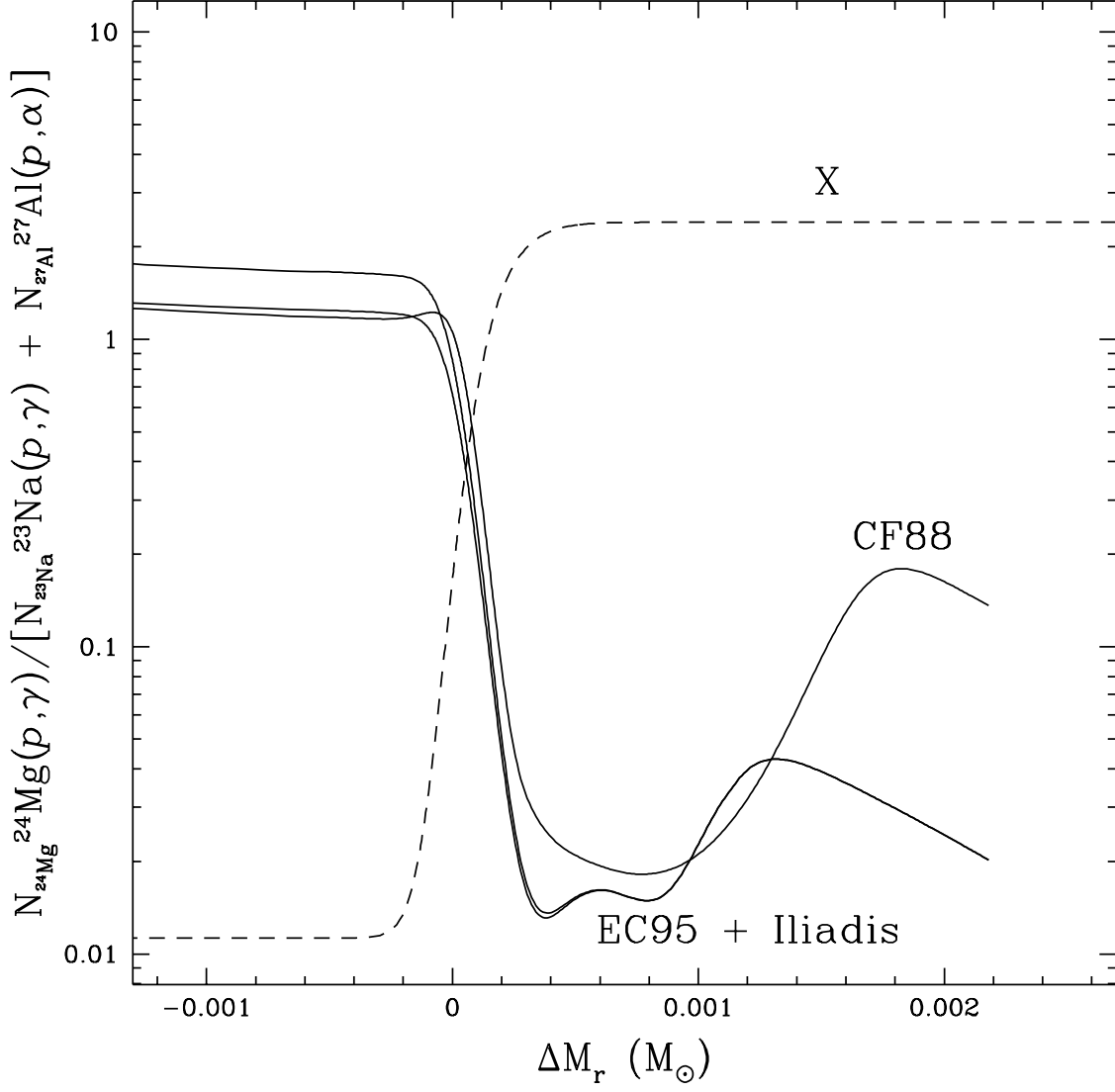


Fig. 23.— A comparison of the destruction-to-production ratio of ^{24}Mg by proton-capture nucleosynthesis for the rates of CF88 and newer results.

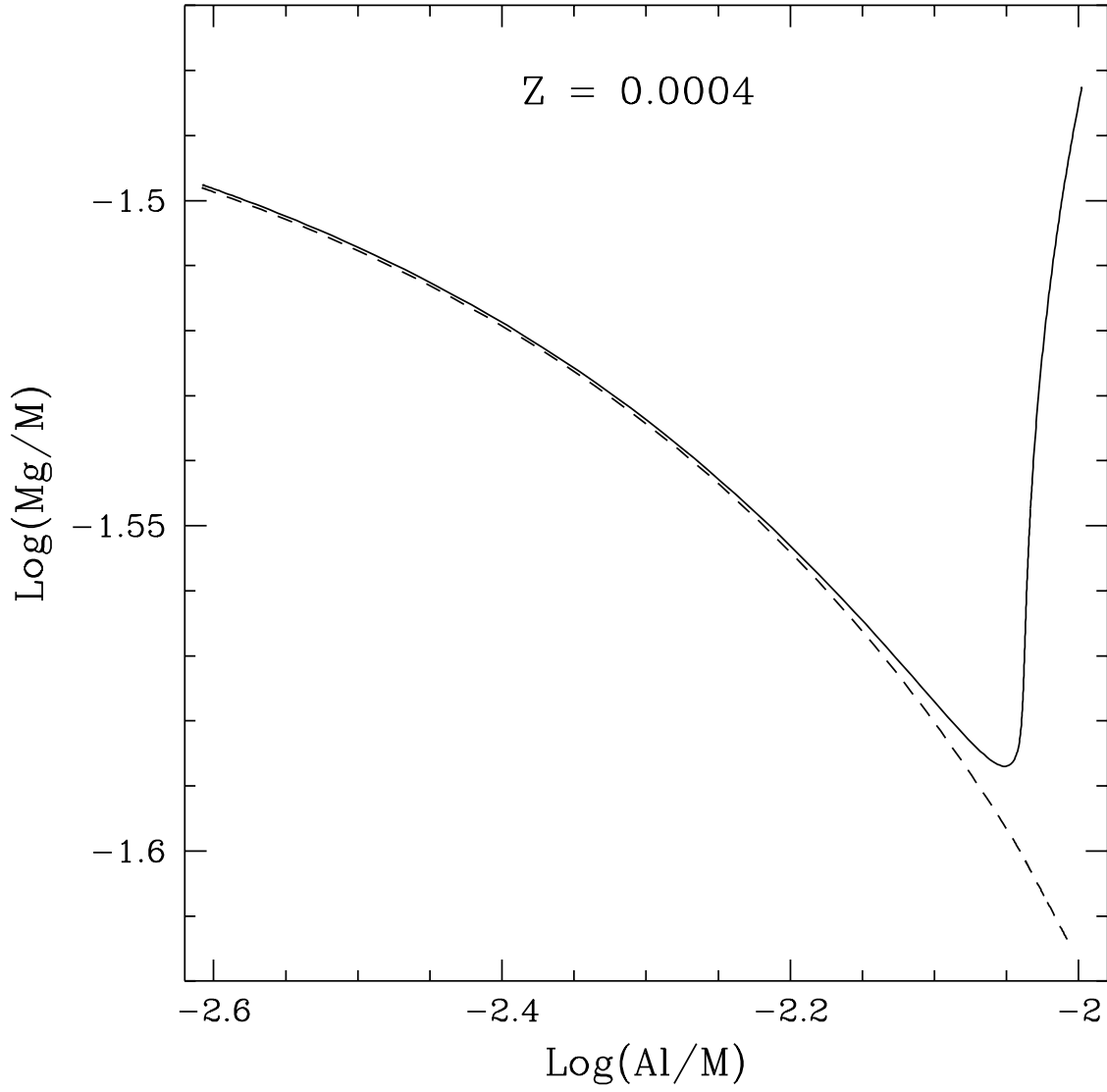


Fig. 24.— Mg vs. Al at the RGB tip of the $Z = 0.0004$ sequence for the EC95 rates chosen in this study (solid line) and for no leakage from the NeNa cycle (dashed line).

at $T_9 = 0.06$. For the ^{26}Mg proton capture reactions, we used the average values from the tables given by Iliadis et al. (1990). The range in uncertainty does not become significant until $T_9 \sim 0.05$ where it spans a factor of ~ 100 . The $^{25,26}\text{Mg}(p, \gamma)$ reactions serve to initially enhance the ^{27}Al abundance at cooler temperatures and ultimately to bridge the reactions between ^{24}Mg and ^{27}Al at higher temperatures. Figure 25 shows the effect of varying the ^{26}Mg proton capture rate between its upper and lower limits for the $Z = 0.0004$ sequence. The average of the limits is about the same as the CF88 rates scaled downward by a factor of ~ 16 at $T_9 = 0.02$ to a factor of ~ 4 near $T_9 = 0.05$. The difference in the resultant abundances is larger on the lower RGB when the H shell is approaching the temperature regime where the difference between the upper and lower limits of the rates becomes significant. Using the upper limits creates 0.22 dex more ^{27}Al at the center of the H shell at the start of mixing in comparison to using the lower limits. The difference in the location around the H shell of where the elements change abundance is more pronounced on the upper RGB, where the now very different limits manifest their sensitivity to the higher temperatures. For example, toward the RGB tip, ^{27}Al becomes enhanced farther above the H shell when the upper limit is used than when the lower limit is used. The result is that the upper limit produces 0.16 dex more ^{27}Al at the top of the H shell ($\Delta S = +1$) at the tip of the RGB. The consequences of both the difference in the production rate and the point of production above the H shell depend on the depth of mixing.

The overall effect of the uncertainty in the ^{26}Mg proton-capture reaction rate is seen in all four sequences. As the metallicity decreases, the uncertainty becomes less important because the temperatures are high enough that the ^{26}Mg is diminished near the top of the H shell for all but the lowest rates. In these cases, all that is necessary to create large overabundances of ^{27}Al is that the ^{26}Mg proton capture proceed more rapidly than the ^{24}Mg proton capture, which it does. This rate will, however, affect the observed Mg isotope ratios, as will the $^{25}\text{Mg}(p, \gamma)^{26}\text{Al}(\beta^+)$ reactions.

Lastly, we explore whether the final two reactions in the MgAl cycle might have important consequences for the abundance of ^{24}Mg . These reactions are the alpha- and gamma-decays of the ^{27}Al proton capture. They determine the cycling nature of the MgAl cycle just as the $^{23}\text{Na}(p, \alpha)$ and (p, γ) reactions do the same for the NeNa cycle. In Paper I we showed how the CF88 rates promote rapid cycling of ^{27}Al back into ^{24}Mg . However, contemporary works of CF88 disputed MgAl cycling at low temperatures and showed the MgAl reactions did, in fact, form a chain (Champagne et al. 1988; Timmermann et al. (1988). In this work, we use the rates generously provided to us by Dr. Christian Iliadis, for both the alpha- and gamma-decay reactions ³. Figure 26 shows the two rates on an

³Dr. Iliadis includes the following comments with his rates: The cycling-to-leakage ratio, which we

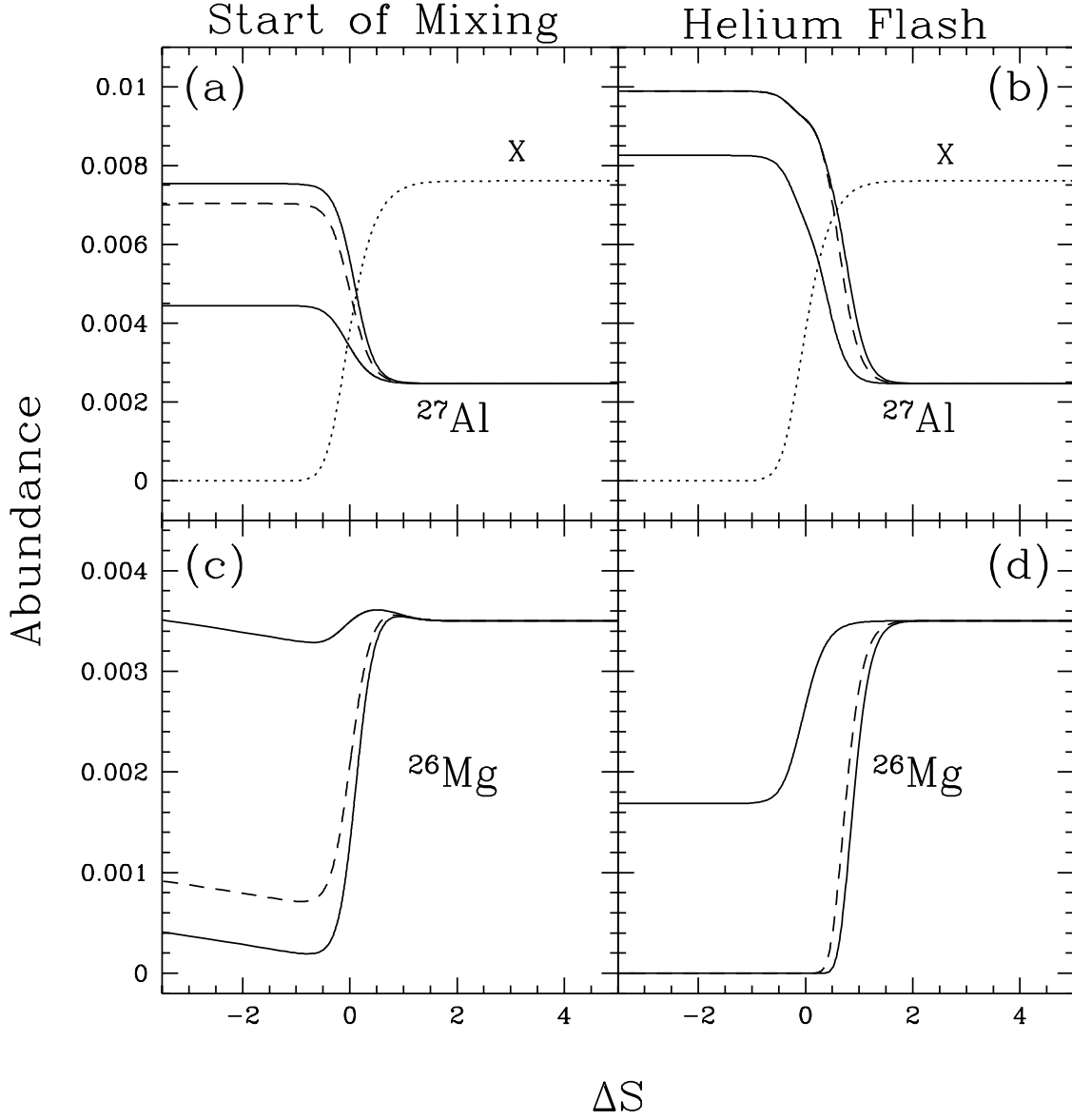


Fig. 25.— The synthesis of ^{27}Al (top panels) and ^{26}Mg (bottom panels) at the start of mixing (left panels) and at the RGB tip (right panels) for the $Z = 0.0004$ sequence. The solid lines represent the range of abundances obtained from the upper and lower limits, the dashed line is the result of using the average of the upper and lower limits of the ^{26}Mg proton-capture rate, and the dotted line is the H-mass fraction scaled by 100.

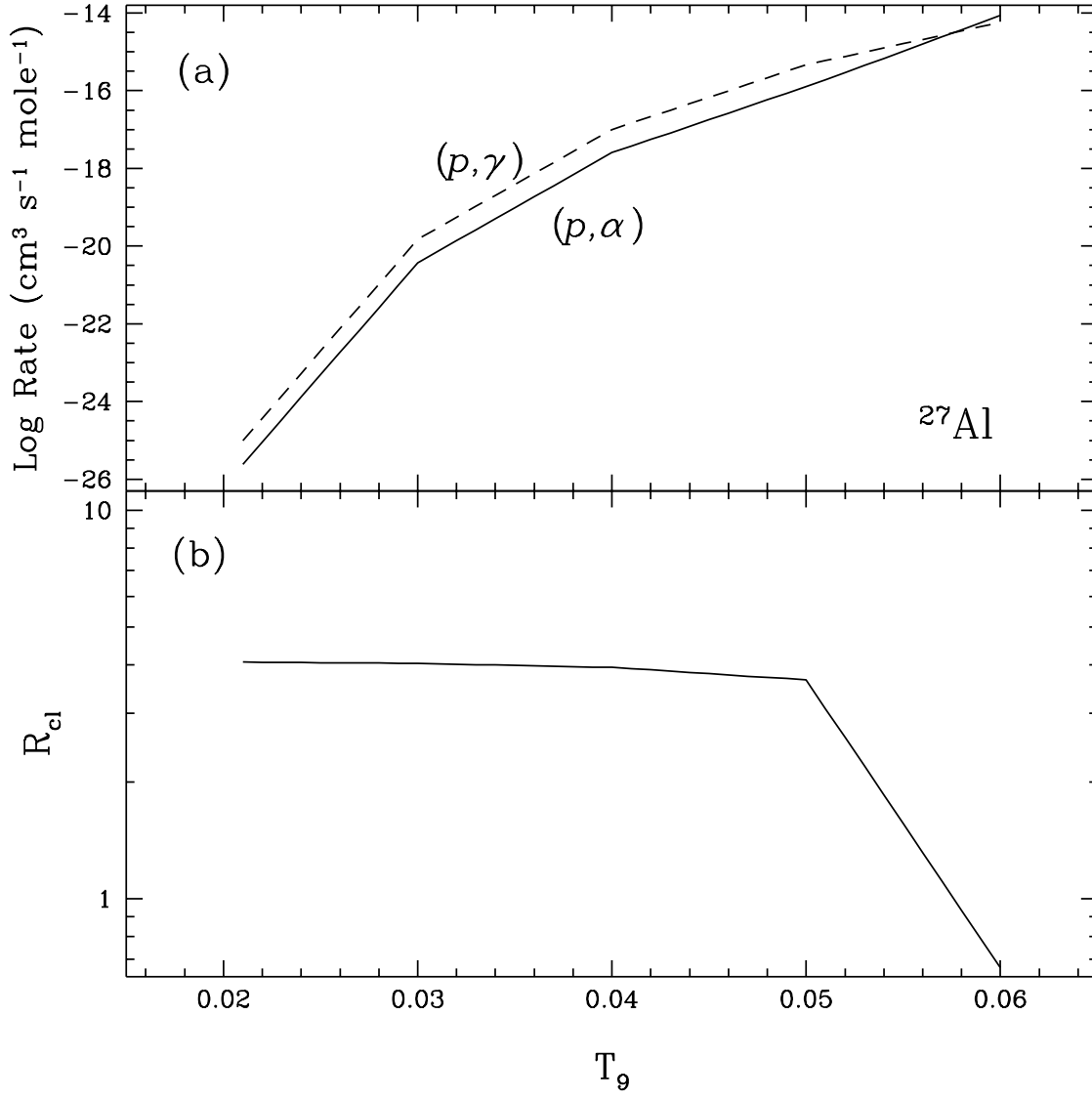


Fig. 26.— (a) The ^{27}Al proton capture rates from Iliadis (1996, private communication). (b) R_{cl} , the α/γ -decay ratio from the rates in panel (a).

absolute scale and their ratio for $T_9 = 0.02 - 0.06$. The top panel indicates that these two rates proceed very slowly at lower temperatures when compared to the lifetime of the RGB. Even at higher temperatures, the destructive proton captures cannot keep pace with the creation of ^{27}Al from the other reactions in the cycle. The bottom panel shows that the cycling-to-leakage ratio, R_{cl} , for the MgAl cycle is weak, even with the upper limits for the alpha decay and the lower limits for the photon decay.

We examine the importance of the cycling reaction on both the ^{24}Mg and ^{27}Al abundance by setting the (p, α) reaction equal to zero. The results are shown in Figure 27 for the model with the highest shell temperature, i.e., the $Z = 0.0001$ sequence at the onset of the helium flash. Clearly the difference in the ^{24}Mg abundance is negligible; there is only a 0.7% reduction at the center of the shell. As a result of no cycling, the ^{27}Al abundance increases by only 1.8%. Even at these hot temperatures, the destruction of ^{24}Mg is not affected by the reactions which complete the MgAl cycle. If its abundance is to be reduced to match the observations in M13 (whose stars theoretically never attain the high temperatures suggested by this model), then another nuclear reaction-rate scenario is needed. We therefore conclude that the overall destruction of ^{24}Mg does not appear to be possible above the center of the H shell according to our present knowledge of the nuclear reaction rates and stellar interiors.

Since (1) totally depleting the $^{25,26}\text{Mg}$, (2) shutting off the leakage from the NeNa cycle, and (3) limiting the cycling in the MgAl cycle do not cause a sufficient enough depletion of ^{24}Mg and enhancement of ^{27}Al above the H shell to match the observations of the brightest M13 giants, we look for an alternative solution. One possibility is presented by Langer, Hoffman, & Zaidins (1996) who suggest that increasing the shell temperature to $T_9 \sim 0.07$ would reproduce these observations. They rely on thermal instabilities in the H-shell to produce the non-canonical temperatures. However, it has been shown (Von Rudloff, VandenBerg, & Hartwick 1988) that the H shell is stable against these thermal perturbations. In addition, by not using evolutionary sequences, they are not able to follow the effect of this extreme temperature on the evolutionary track of a star. A temperature of $T_9 = 0.07$ would require the hottest model for the $Z = 0.0004$ sequence to increase its temperature by nearly 1.4×10^7 K. This would result in a ~ 1.6 dex increase in the luminosity of the RGB tip for this sequence. Thus, we rule out their conclusion as

denote as R_{cl} , probably depends mostly on the contributions of the $E_R = 72$ keV and 85 keV (where E_R is the resonance energy) resonances in the ^{28}Si nucleus. If the reactions proceed only through the 85 keV resonance, then R_{cl} is ~ 0.66 . If the contribution from the 72 keV resonance is significant, then R_{cl} is closer to 4, as shown in Figure 26b. The ratio is better determined than the absolute values of the rates due to the difficulties in measuring very small ($\sim 10^{-15}$ eV) proton partial widths at the low energies found in the H shell. He estimates that the uncertainties in the absolute magnitudes of the rates are at least a factor of ten.

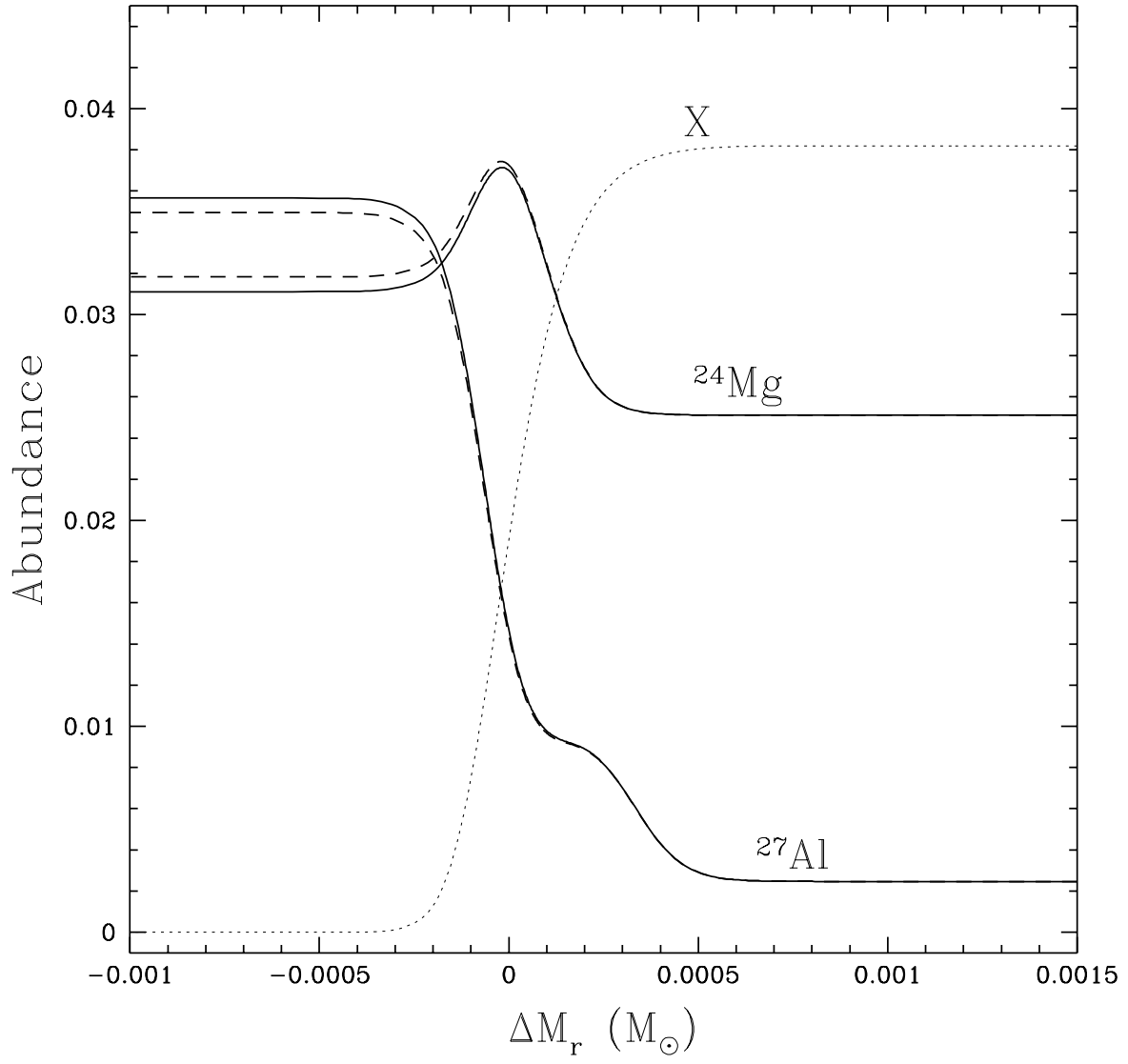


Fig. 27.— The ^{24}Mg and ^{27}Al yields with cycling (dashed line) and no cycling (solid line). The dotted line is the H-mass fraction scaled by a factor of 20.

inconsistent with the observed color-magnitude diagrams of globular clusters.

Instead, we explore what changes in the ^{24}Mg proton-capture rate would be sufficient to match these limited observations. Zaidins & Langer (1997) suggest that theoretically, there is room for a factor of 35 increase in the ^{24}Mg proton-capture rate based on a poorly known width of the lowest resonance at 2468 keV in ^{25}Al . In Figure 28 we present the effect of increasing this rate by various amounts on the one model which most closely resembles the brightest M13 giants. The top panel demonstrates that in order to reduce the total Mg abundance by 0.4 dex to match the observations, the ^{24}Mg proton-capture rate would need to be increased by at least a factor of 35, assuming that all the other reactions which produce ^{24}Mg are unchanged. The corresponding increase in $[\text{Al}/\text{M}]$ is about 1.1 dex, which agrees well with the observations. However, this requires that mixing penetrates to the base of the H shell. The resultant Al abundance from ^{24}Mg is less sensitive to the ^{24}Mg proton-capture rate than the ^{24}Mg abundance; there is approximately a 0.1 dex difference in the ^{27}Al production for each rate at the base of the H shell. At a mixing depth of say 20% H depletion, the change in the total Mg abundance for the factor of 50 increase in the ^{24}Mg proton-capture rate is not distinguishable from having no increase in the rate. The questions which remain to be answered are (1) how much of an increase in the $^{24}\text{Mg}(p, \gamma)^{25}\text{Al}$ reaction is possible, and (2) how deeply into the H shell can the mixing realistically penetrate? At this point the best we can say about the first question is that the rate probably needs to be substantially increased in the H shell temperature range. Whether this can happen is currently being considered (Iliadis, private communication). The second question will be explored in better detail once mixing is studied in these sequences.

7. Discussion

We have combined a nuclear reaction network with detailed stellar models in order to follow the evolution of the light abundances around the H shell of globular cluster RGB stars. In so doing, we have qualitatively reproduced many of the observations which show luminosity- and metallicity-dependent variations in the abundances of C, N, O, Na, Mg, and Al. We conclude this work with a synopsis of the results with an eye towards further work which will incorporate a mixing algorithm into our calculations.

From the stellar physics, we conclude that both the metallicity and luminosity of a star play an important role in determining the surface abundances. We have shown: (1), that τ_{shell} decreases with increasing metallicity. This allows less time for the nuclear burning to alter the internal abundances before the H shell overtakes the processing region. (2), the more metal-rich sequences have steeper temperature gradients creating more

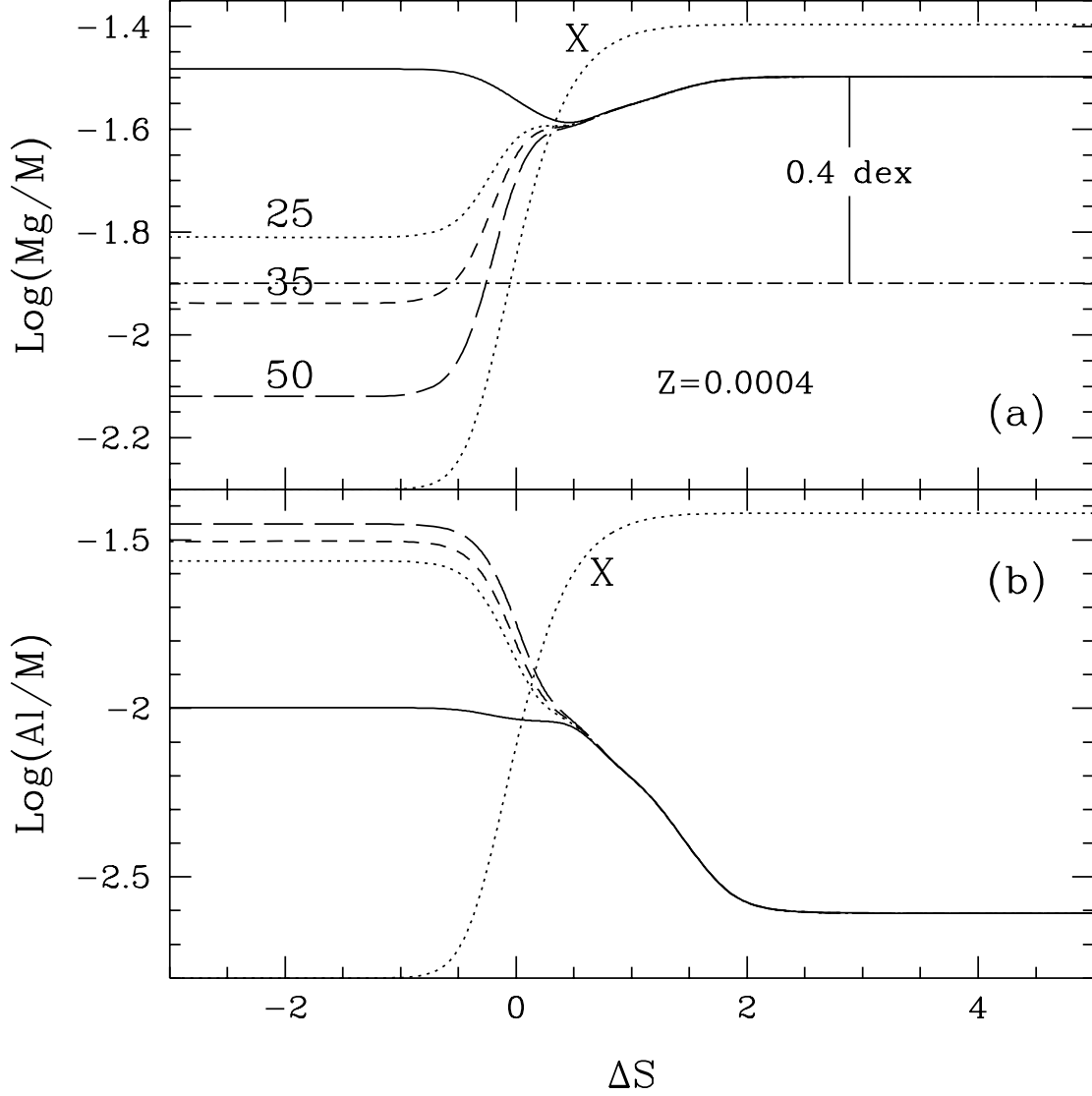


Fig. 28.— The change in the total Mg (top panel) and Al (bottom panel) abundances in the RGB tip model of the $Z = 0.0004$ sequence as a consequence of increasing the $^{24}\text{Mg}(p, \gamma)^{25}\text{Al}$ reaction rate of CF88 by a factor of 25, 35, and 50. The dotted line traces the H shell. The dot-dashed line in panel (a) indicates a depletion of 0.4 dex in the total Mg abundance relative to the envelope value.

narrow burning regions. And (3), these sequences burn at lower temperatures around the H shell and therefore do not experience all the reactions that the lower-metallicity sequences can. These three points lead to the conclusion that the low-metallicity sequences should experience greater variations in their surface abundances in more elements than the high-metallicity sequences, assuming mixing does occur.

Within a given sequence, the stellar physics leads to similar conclusions. As a star evolves, τ_{shell} decreases and the processing regions contract. This, by itself, would tend to reduce the amount of matter that can be mixed. Competing with this in the higher-luminosity models is a higher temperature which can cause more matter to be processed on a shorter timescale. In addition, the higher temperatures of the brighter models cause some nuclear reactions to occur that were not possible on the lower RGB. Thus, we expect to see luminosity dependent variations within a given sequence, with the extent depending heavily on the mixing parameters.

As our models show no changes in the abundances of any element heavier than ^{27}Al , we discuss the changes one might expect to see in the CNO-, NeNa-, and MgAl-cycle isotopic abundances as a function of luminosity and metallicity. We have shown that there exists two separate regions above the H shell in which ^{12}C and ^{16}O are depleted at all luminosities and metallicities. Therefore, stars which undergo mixing on the RGB should exhibit a C vs. N and perhaps a O vs. N anticorrelation regardless of metallicity. The mixing parameters could prevent the products of the O-N conversion from being brought to the surface in some higher-metallicity stars where the O-N processed region is small compared to the C-depleted region. The one ubiquitous conclusion which we can make is that, irrespective of metallicity, any star which shows C variations due to mixing should also exhibit a low $^{12}\text{C}/^{13}\text{C}$ ratio. In addition, any star which shows O variations due to mixing should also show a $^{16}\text{O}/^{17}\text{O}$ ratio near its equilibrium value, or slightly smaller due to the immediate increase in ^{17}O from ^{16}O at the onset of O depletion. According to the new ^{17}O proton-capture rates of Blackmon et al. (1995) this value is between 50 and 150 and should peak at brighter luminosities. Currently, there are no O isotope data for globular clusters. Perhaps observations of this quantity in stars which show large O depletions that would indicate mixing into the O equilibrium region, such as the super O-poor stars in M13 seen by KSLS93, can help constrain these rates. We submit that the ^{17}O abundance might best be seen from the $^{12}\text{C}^{17}\text{O}$ IR system at $2.3\ \mu\text{m}$ and $4.6\ \mu\text{m}$ (Balachandran, private communication).

As for the NeNa cycle abundances, we conclude that all the sequences are capable of showing some Na enhancements as a result of a single proton capture on ^{22}Ne . This occurs nearer to the surface than the O-depleted region for lower luminosity models independent

of metallicity and eventually overlaps the O shell as the sequence evolves. Depending on the mixing depth, this can result in a slight increase in ^{23}Na with little variation in O. Slightly deeper mixing, especially in brighter models, should cause an anticorrelation between Na and O. Extra-Na enhancements from ^{20}Ne are seen inside the O-depleted region when mixing begins for the $Z = 0.0001$ and $Z = 0.0004$ sequences. The $Z = 0.004$ sequence shows larger Na enhancements from the NeNa cycle only after the onset of mixing, and the $Z = Z_{\odot}$ sequence exhibits hardly any NeNa-cycle processing. Thus, we anticipate that the lower-metallicity stars might exhibit large Na enhancements if they also show large O depletions. Higher-metallicity stars, however, which show large O depletions at lower luminosities might not have large Na enhancements until they evolve further up the RGB. Even then, the mixing would have to be very deep (near the center of the H shell) and would have to compete with a decreasing τ_{shell} .

We also explore the cycling nature of the NeNa cycle using the new rates of EC95 compared to the more widely used rates of CF88. We find that the EC95 rates promote leakage from the cycle at four times the rate promoted by CF88 for $0.04 \lesssim T_9 \lesssim 0.06$, with little variation caused by the uncertain resonances in the (p, γ) and (p, α) reactions. This causes an increase in the ^{24}Mg abundance at higher temperatures despite it being depleted to create ^{27}Al .

Finally, we discuss the MgAl cycle elements. These change only inside the O-depleted region and should be correlated with a diminution of O and an enhancement of N. The abundance yields for these elements are very sensitive to temperature as manifested by both luminosity and metallicity. To begin, ^{27}Al is produced by all three Mg isotopes. In the $Z = Z_{\odot}$ sequence, it comes solely from proton captures on ^{26}Mg and only near the tip of the RGB. For the same sequence, the meta-stable isotope ^{26}Al is produced directly from ^{25}Mg , and decays into ^{26}Mg as it is overtaken by the H shell. Assuming sufficiently quick (τ_{mix} less than the decay lifetime of ^{26}Al) and deep ($\Delta S \sim 0$) mixing for such a sequence, we would anticipate a large depletion of the ^{25}Mg abundance, a minor depletion of the ^{26}Mg abundance that is correlated with a slight enhancement of ^{27}Al , and no change in ^{24}Mg at all RGB luminosities. However, if the mixing is slower, we would expect the ^{25}Mg abundance to be depleted completely into ^{26}Mg , resulting in a possible enhancement of ^{26}Mg despite the slight increase in ^{27}Al . As the metallicity decreases to $Z = 0.004$, the ^{27}Al production starts to come more from both ^{25}Mg and ^{26}Mg . Again though, there is no change in the ^{24}Mg abundance.

We have shown that we are sensitive to the ^{26}Mg proton-capture rate above the top of the H shell for all metallicities. Both the upper and lower limits produce a significant amount of ^{27}Al , but at slightly different depths. Thus, ^{26}Mg variations depend strongly

on the depth of mixing and further quantitative analysis shall have to wait until mixing is invoked.

The two lower-metallicity sequences show the largest changes in the ^{27}Al abundance. Due in part to the relatively large value of τ_{shell} , all the ^{25}Mg and ^{26}Mg is converted into ^{27}Al even at the start-of-mixing luminosity. As the sequence evolves, the ^{27}Al abundance increases dramatically within the H shell from proton captures on ^{24}Mg in the MgAl cycle. Not all of this extra Al is likely to be reached by the mixing currents since it occurs in a region of large H depletion. Thus, the Al variation is very dependent on the mixing parameters. At this point, we can only conclude that lower metallicity sequences ($Z \lesssim 0.0004$) should exhibit large Al enhancements that should correlate with a diminution of $^{25,26}\text{Mg}$ and perhaps ^{24}Mg .

The most difficult puzzle to solve is that of the observed ^{24}Mg abundances in the M13 RGB and NGC 6752 tip stars. According to our sequence at the relevant metallicity, we would expect no depletion of ^{24}Mg in the same region of Al enhancements above the center of the H shell, despite ^{24}Mg being the source of the Al over-production. This is because the EC95 rates provide sufficient leakage from the NeNa cycle into ^{24}Mg to more than account for its depletion. We showed in Paper I that even the “standard” CF88 rates predict a marginal increase in the ^{24}Mg abundance due to leakage. To reconcile our models with the observations we have tried limiting the NeNa leakage by both taking its published lower limit and by shutting it off completely. We have also tried stopping the cycling reaction in the MgAl cycle. None of these procedures had much impact on the ^{24}Mg abundance at realistic H depletions. In order to decrease the ^{24}Mg abundance by the observed amount, it is necessary to increase significantly the ^{24}Mg proton-capture rate and to mix deeply into the H shell. Finally, we rule out as a possible solution any dramatic increases in the shell temperature since this would contradict the observed RGB tip luminosity. We are thus left in a quandary about how to approach the ^{24}Mg anomalies. This is clearly a problem whose resolution requires further observations, investigation into the ^{24}Mg proton-capture rate, and the addition of mixing into the sequences.

Putting the ^{24}Mg uncertainties aside, we note that the proximity of the large Al enhancements to the H shell and the observational evidence which supports mixing to this depth would indicate that some fraction of He must also be mixed to the surface. If the extra mixing of He is a contributing factor of the blue horizontal branches (HB) in some clusters as suggested by Langer & Hoffman (1995) and verified though extensive modeling by Sweigart (1997a,b), then one would expect these “second-parameter” clusters to be super-abundant in Al. Indeed, M13 (Kraft et al. 1997) and NGC 6752 (Shetrone 1997) fit this criteria. This prediction can be further tested by searching for Al in clusters with

similar metallicity to these clusters but with redder HB's, such as M3 and M5. In fact, both M3 and M5 show less severe O depletions than M13 (Snedden et al. 1992; KSLP92), which would indicate less severe mixing. If the Al is anticorrelated with O, then M3 and M5 should not have the large Al enhancements or the ^{24}Mg depletions seen in M13.

Pilachowski & Sneden (1983) observed that NGC 288 has a very blue HB for its metallicity ($[\text{Fe}/\text{H}] = -1.0$). This might indicate the presence of deep mixing. However, based on our results, a cluster this metal-rich would not be expected to over-produce Al because it never attains high enough temperatures to burn ^{24}Mg . Thus, the most one might expect to observe in NGC 288 if deep mixing is bringing He up to the surface to create the blue HB, is a slight increase in ^{27}Al at the expense of $^{25,26}\text{Mg}$.

Future work will involve subjecting these sequences to a mixing algorithm and the results will be reported elsewhere. Having accomplished this, we will explore the abundances of other isotopes such as ^3He and ^7Li which have significant cosmological implications. (see, e.g., Spite & Spite 1982; Charbonnel 1996)

We wish to thank Dr. David Arnett for allowing us the use of his nuclear reaction network. We express our gratitude and indebtedness to Dr. Christian Iliadis for his thoughtful discussions of our nuclear reaction network and for his encouragement of our study of the effects of the uncertainties in the rates on our results. It is also our pleasure to thank the members of Triangle Universities National Laboratory, particularly Ms. Denise Powell and Mr. Steve Hale, for their careful experiments regarding the nuclear reaction rates in the NeNa and MgAl cycles. We thank Dr. John Norris for his useful comments on our work prior to the writing of this manuscript and Dr. Bruce Carney for his insightful comments regarding Na and O abundances. And for keeping us well informed of their latest observational data, Dr. Michael Briley, Dr. Matthew Shetrone and Dr. Caty Pilachowski are gratefully acknowledged. We also thank the referee for his/her careful reading of our manuscript and for the constructive comments which helped form the final draft of this work. The work of A.V.S. is funded in part by NASA grant NAG5-3028 and that of R.A.B. by NSF AST93-14931 and NASA grant NAG5-3028. Finally, R.M.C. wishes to acknowledge the NASA Graduate Student Research Program for financial support of his research.

REFERENCES

- Anders, E. & Grevesse, N. 1989, *Geochim. Cosmochim. Acta*, 53, 197
- Anthony-Twarog, B. J., Twarog, B. A., & Craig, J. 1995, *PASP*, 107, 32
- Bell, R. A. & Dickens, R. J. 1980, *ApJ*, 242, 657
- Bell, R. A., Dickens, J. A., & Gustafsson, B. 1979, *ApJ*, 229, 604
- Bell, R. A., Hesser, J. E., & Cannon, R. D. 1983, *ApJ*, 269, 580
- Bell, R. A., Hesser, J. E., & Cannon, R. D. 1983, *ApJ*, 283, 615
- Blackmon, J. C., Champagne, A. E., Hofstee, M. A., Smith, M. S., Downing, R. G., & Lamaze, G. P. 1995, *Phys. Rev. Lett.*, 74, 2642
- Briley, M. M. 1997, *AJ*, 113, 306
- Briley, M. M., Bell, R. A., Smith, G. H., & Hesser, J. E. 1989, *ApJ*, 341, 800
- Briley, M. M., Bell, R. A., Hesser, J. E., & Smith, G. H. 1994, *Can. J. Phys.*, 72, 772
- Briley, M. M., Bell, R. A., Hoban, S., & Dickens, R. J. 1990, *ApJ*, 359, 307
- Briley, M. M., Hesser, J. E., & Bell, R. A. 1991, *ApJ*, 373, 482
- Briley, M. M., Smith, G. H., Bell, R. A., Oke, J. B., & Hesser, J. E. 1992, *ApJ*, 387, 612
- Briley, M. M., Smith, V. V., Lambert, D. L 1994, *ApJ*, 424, L119
- Briley, M. M., Smith, V. V., Suntzeff, N. B., Lambert, D. L, Bell, R. A., & Hesser, J. E. 1996, *Nature*, 383, 604
- Briley, M. M., Suntzeff, N. B., Smith, V. V., Bell, R. A., & Norris, J. 1997, *BAAS*, 28, 1363
- Brown, J. A., Wallerstein, G., & Oke, J. B. 1991, *AJ*, 101, 1693
- Carbon, D. F. et al. 1982, *ApJS*, 49, 207
- Caughlin, G. R. & Fowler, W. A. 1988, *Atom. Data and Nuc. Data Tables*, 40, 283 (CF88)
- Cavallo, R. M., Sweigart, A. V., & Bell, R. A. 1996, *ApJ*, 464, L79 (Paper I)
- Champagne, A. E. et al. 1988, *Nucl. Phys. A*, 487, 433
- Charbonnel, C. 1994, *A&A*, 282, 811
- Charbonnel, C. 1995, *ApJ*, 453, L41
- Charbonnel, C. 1996, in *From Stars to Galaxies: The Impact of Stellar Physics on Galaxy Evolution*, eds. C. Leitherer, U. Fritze-v., and J. Huchra, (San Francisco: ASP), p. 213

- Clayton, D. D. 1983, *Principles of Stellar Evolution and Nucleosynthesis* (New York: McGraw-Hill)
- Cohen, J. G. 1978, *ApJ*, 223, 487
- Cottrell, P. L. & Da Costa, G. S. 1981, *ApJ*, 245, L79
- Da Costa, G. S. & Cottrell, P. L. 1980, *ApJ*, 236, L83
- Denisenkov, P. A. & Denisenkova, S. N. 1990, *Sov. Astron. Lett.*, 16, 275
- Denissenkov, P. A. & Weiss, A. 1996, *A&A*, 308, 773
- Dickens, R. J. & Bell, R. A. 1976, *ApJ*, 207, 506
- Dickens, R. J., Croke, B. F. W., Cannon, R. D., & Bell, R. A. 1991, *Nature*, 351, 212
- Drake, J. J., Smith, V. V., & Suntzeff, N. B. 1992, *ApJ*, 396, L95
- El Eid, M. F. & Champagne, A. E. 1995, *ApJ*, 451, 298 (EC95)
- Fusi Pecci, F., Ferraro, F. R., Crocker, D. A., Rood, R. T., & Buonanno, R. 1990, *A&A*, 238, 95
- Gilroy, K. K. & Brown, J. A. 1991, *ApJ*, 371, 578
- Hesser, J. E. 1978, *ApJ*, 223, L117
- Hesser, J. E., Hartwick, F. D. A., & McClure, R. D. 1977, *ApJS*, 33, 471
- Iliadis, C. et al. 1990, *Nucl. Phys. A*, 512, 509
- Iliadis, C., Buchmann, L., Endt, P. M., Herndel, H., & Weischer, M. 1996, *Phys. Rev. C*, 53, 475
- Kraft, R. P. 1994, *PASP*, 106, 553
- Kraft, R. P., Sneden, C., Smith, G. H., Shetrone, M. D., Langer, G. E., & Pilachowski, C. A. 1997, *AJ*, 113, 279
- Kraft, R. P., Sneden, C., Langer, G. E., & Prosser, C. F. 1992 *AJ*, 104, 645 (KSLP92)
- Kraft, R. P., Sneden, C., Langer, G. E., & Shetrone, M. D. 1993, *AJ*, 106, 1490 (KSLS93)
- Landré, V., Prantzos, N., Aguer, P., Bogaert, G., Lefebvre, A., & Thibaud, J. P. 1990, *A&A*, 240, 85
- Langer, G. E. & Hoffman, R. D. 1995, *PASP*, 107, 1177
- Langer, G. E., Hoffman, R., & Sneden, C. 1993, *PASP*, 105, 301
- Langer, G. E., Hoffman, R., & Zaidins, C. 1996, *PASP*, 109, 244
- Langer, G. E., Kraft, R. P., Carbon, D. F., & Friel, E. 1986, *PASP*, 98, 473

- Langer, G. E., Kraft, R. P., & Friel, E. D. 1985, *PASP*, 97, 373
- Norris, J. 1981, *ApJ*, 248, 177
- Norris, J., Cottrell, P. L., Freeman, K. C., & Da Costa, G. S. 1981, *ApJ*, 244, 205
- Norris, J. E. & Da Costa, G. S. 1995a, *ApJ*, 447, 680
- Norris, J. E. & Da Costa, G. S. 1995b, *ApJ*, 441, L81
- Norris, J. E. & Freeman, K. C. 1979, *ApJ*, 230, L179
- Norris, J. & Smith, G. H. 1984, *ApJ*, 287, 255
- Paltoglou, G. & Norris, J. E. 1989, *ApJ*, 336, 185
- Peterson, R. C. 1980, *ApJ*, 237, L87
- Pilachowski, C. A. 1988, *ApJ*, 326, L57
- Pilachowski, C. A. & Sneden, C. 1983, *PASP*, 95, 229
- Pilachowski, C. A., Sneden, C., Kraft, R. P., & Langer, G. E. 1996, *AJ*, 112, 545 (PSKL96)
- Richard, O., Vauclair, S., Charbonnel, C., & Dziembowski, W. A. 1996, *A&A*, 312, 1000
- Shetrone, M. D. 1995, *BAAS*, 27, 1432
- Shetrone, M. D. 1996a, *AJ*, 112, 1517
- Shetrone, M. D. 1996b, *AJ*, 112, 2639
- Shetrone, M. D. 1997, in *Poster Proceedings of IAU Symposium 189: The Interaction between Observations and Theory*, T. R. Bedding, ed. (Sydney: University of Sydney)
- Smith, G. H. & Bell, R. A. 1986, *AJ*, 91, 1121
- Smith, G. H., Bell, R. A., & Hesser, J. E. 1989, *ApJ*, 341, 190
- Smith, G. H. & Mateo, M. 1990, *ApJ*, 353, 533
- Smith, G. H. & Norris, J. 1983, *ApJ*, 264, 215
- Smith, G. H., Shetrone, M. D., Bell, R. A., Churchill, C. W., & Briley, M. M. 1996, *AJ*, 112, 1511
- Smith, G. H., Shetrone, M. D., Briley, M. M., Churchill, C. W., & Bell, R. A. 1997, *PASP*, 109, 236
- Smith, G. H. & Wirth, G. D. 1991, *PASP*, 103, 1158
- Smith, V. V. & Suntzeff, N. B. 1989, *AJ*, 97, 1699
- Sneden, C., Kraft, R. P., Langer, G. E., Prosser, C. F., & Shetrone, M. D. 1994, *AJ*, 107, 1773

- Snedden, C., Kraft, R. P., Prosser, C. F., & Langer, G. E. 1991, *AJ*, 102, 2001
- Snedden, C., Kraft, R. P., Prosser, C. F., & Langer, G. E. 1992, *AJ*, 104, 2121
- Spite, F. & Spite, M. 1982, *A&A*, 115, 357
- Suntzeff, N. B. 1981, *ApJS*, 41, 1
- Suntzeff, N. B. & Smith, V. V. 1991, *ApJ*, 381, 160
- Sweigart, A. V. 1997a, *ApJ*, 474, L23
- Sweigart, A. V. 1997b, in *The Third Conference on Faint Blue Stars*, eds. A. G. D. Philip, J. W. Liebert, and R. A. Saffer, (Schenectady: L. Davis Press), p. 3
- Sweigart, A. V. & Mengel, J. G. 1979, *ApJ*, 229, 624 (SM79)
- Timmermann, R., Becker, H. W., Rolfs, C., Schröder, U., & Trautvetter, H. P. 1988, *Nucl. Phys. A*, 477, 105
- Trefzger, C. F., Carbon, D. F., Langer, G. E., Suntzeff, N. B., & Kraft, R. P. 1983, *ApJ*, 266, 144
- VandenBerg, D. A. & Smith, G. H. 1988, *PASP*, 100, 314
- Von Rudloff, I. R., VandenBerg, D. A., & Hartwick, F. D. A. 1988, *ApJ*, 324, 840
- Zaidins, C. S. & Langer, G. E. 1997, *PASP*, 109, 252

Table 1. Properties of the RGB Sequences

Z	[Fe/H]	Y	M (M_{\odot})	Log L_{mix} ^a (L_{\odot})	$M_{\text{sh,mix}}$ ^b (M_{\odot})	Log L_{tip} ^c (L_{\odot})	$M_{\text{sh,tip}}$ ^d (M_{\odot})	τ_{RGB} ^e (Myr)	t_{tip} ^f (Gyr)	Models Selected ^g
0.0001	−2.27	0.230	0.795	2.28	0.356	3.22	0.501	20.8	15.0	31
0.0004	−1.67	0.230	0.800	2.11	0.325	3.26	0.492	29.1	15.1	36
0.004	−0.67	0.230	0.875	1.72	0.273	3.33	0.483	58.7	14.9	44
0.01865	0.00	0.2825	1.500	1.83	0.272	3.34	0.464	40.5	2.7	40

^aThe luminosity at the start of mixing.

^bThe mass coordinate M_r at the center of the H shell at the start of mixing.

^cThe luminosity at the tip of the RGB.

^dThe mass coordinate M_r at the center of the H shell at the tip of the RGB.

^eThe lifetime on the RGB between the start of mixing and the He flash.

^fThe sequence age at the tip of the RGB.

^gThe number of models from each sequence in which the abundance profiles were calculated.